

---

# 10

---

## TRAVELING-WAVE ANTENNAS

Traveling-wave antennas consist of transmission-line structures that radiate. We develop a unified theory for end-fire line antennas because length and propagation constant along the structure determine most of their properties. To first order, length determines gain and bandwidth. The size and shape of the structure produce secondary effects such as polarization nulls and narrower beamwidths. Most of these structures are slow wave-transmission structures that bind waves to it and radiate at discontinuities. We use surface-wave structures to radiate end-fire beams and leaky wave structures to radiate beams at an angle to the axis of the line source. In both cases there are planar configurations that have their uses, but in this chapter we concentrate on long, thin geometries. We combine leaky wave line-source radiators, such as slotted rectangular waveguides, into planar arrays, but the line source remains the building block.

We make traveling-wave antennas from structures that guide waves. Surface-wave structures bind the power to the transmission line and radiate from discontinuities such as bends or dimensional changes. In some cases we analyze the surface wave as radiating throughout its extent on the transmission line. Both methods provide insight. Leaky wave antennas carry waves internally, such as a waveguide, and radiate at openings that allow power to escape. The radiation mechanism differs in the two cases, but we use similar mathematics to describe both types. We may have trouble distinguishing the radiation mode because the structures may be similar because with small changes in structure, some antennas can radiate in either mode. We separate traveling-wave antennas from other antennas by the presence of a wave traveling along the structure, with most of its power propagating in a single direction.

We divide antennas by their structure: line and planar. We usually analyze planar structures as being infinite in the direction normal to the wave propagation. Similarly, we usually ignore the diameter of line sources in a first-order analysis. The diameter is important for determining the mode structure, but to first order we calculate patterns

based on a thin line source since length and propagation constant determine the pattern and bandwidth. The width of a planar structure determines the pattern beamwidth in that plane. Increasing the diameters of the rods of line sources will decrease the pattern beamwidth and increase gain, but the effect is secondary. Only when we include the diameter can we make the transition to aperture-type structures considered to be radiating from the end.

In this chapter we must consider unusual transmission-line structures. Properly designed dimensions provide the proper phase velocity to establish a single end-fire beam for slow-wave antennas or to point the beam of a leaky wave antenna. We calculate some of the dimensions by analysis (an ever-expanding list), but we can also measure the velocities and leakage and proceed to design.

## 10-1 GENERAL TRAVELING WAVES

A wave traveling in a single direction has a field representation:

$$E = E_0(z)e^{-kPz} \quad (10-1)$$

where  $z$  is the direction of propagation,  $k$  the free-space propagation constant (wave number)  $2\pi/\lambda$ , and  $P$  the relative propagation constant.  $E_0(z)$  describes the amplitude variation:

$$\begin{aligned} P > 1 & \quad \text{surface waves} \\ P < 1 & \quad \text{leaky waves} \end{aligned} \quad (10-2)$$

For a planar structure in the  $y$ - $z$  plane, we consider separable distributions:

$$E = E_0(z)E_1(y)e^{-jkPz}$$

We compute the pattern from

$$f = \int_0^L \int_{-a}^a E_0(z)E_1(y)e^{-jkPz}e^{jk_z z}e^{jk_y y}dzdy \quad (10-3)$$

where  $k_z = k \cos \theta$ . Similarly, for circular distributions we have

$$E = E_0(z)E_1(\phi)e^{-jkPz}$$

and

$$f = \int_0^L E_0(z)e^{-jkPz}e^{jk_z z}dz \int_0^{2\pi} E_1(\phi_c)a e^{jka \sin \theta \cos(\phi - \phi_c)}d\phi_c \quad (10-4)$$

where  $a$  is the radius. The second integral includes vector dot products to project the ring aperture fields on to the far-field polarizations (see Section 7-2). We consider only the term along the  $z$ -axis, and we can consider the effect of the other coordinate separately. The pattern response is

$$f = \int_0^L E_0(z)e^{-jk_z(P - \cos \theta)}dz \quad (10-5)$$

We use the results of Chapter 4 with these separable distributions. Maximum gain comes from a uniform distribution reduced by the amplitude taper efficiency for tapered distributions. In Eq. (10-3) the  $y$ -axis distribution and size determine the gain factor as a product for aperture area. Equation (10-4) has a separable  $\phi$  distribution that separates directivity into a product. We ignore these factors for now and concentrate on the  $z$ -axis pattern and associated directivity. Linear-rod antennas have increased directivity because of dipole  $\phi$  distributions and their increased radius.

A traveling wave with a uniform distribution has pattern response

$$\frac{\sin(\psi/2)}{\psi/2} \quad \text{where} \quad \psi = kL(P - \cos \theta) \quad (10-6)$$

for  $\theta$  measured from the  $z$ -axis. The  $y$  or  $\phi$  distribution determines the pattern in the other coordinate. For  $P > 1$ , a slow wave, the beam peak approaches  $\theta = 0$  when  $P \rightarrow 1$ . The length bounds the range  $P$  for an end-fire pattern peak. Leaky waves,  $P < 1$ , have a pattern peak when  $P = \cos \theta$ , or

$$\theta_{\max} = \cos^{-1} P \quad (10-7)$$

The pattern peak approaches end fire ( $\theta = 0$ ) as  $P \rightarrow 1$ . By increasing  $P$  beyond 1, the directivity increases and reaches maximum value for a given  $P$ , depending on the length [1]

$$P = 1 + \frac{0.465}{L} \quad (10-8)$$

Equation (10-8) is the Hansen and Woodyard criterion for increased directivity of a long end-fire structure commonly approximated by [2]

$$P = 1 + \frac{1}{2L} \quad (10-9)$$

The phase increase of  $180^\circ$  [Eq. (10-9)] along the length gives the maximum directivity for a long structure with a uniform distribution. The amplitude distribution for most surface-wave devices ( $P > 1$ ) peaks near the input and the taper reduces the gain by the amplitude taper efficiency [Eq. (4-8)]. We reduce the relative propagation constant from that given by Eq. (10-8) depending on the length [3]:

$$P = 1 + \frac{1}{RL} \quad (10-10)$$

where  $R = 6$  at  $L = \lambda$ , diminishing to 3 from  $L = 3\lambda$  to  $L = 8\lambda$  and tapering to 2 [Eq. (10-9)] at  $L = 20\lambda$ . Zucker [4] uses  $R = 6$  for the amplitude, which peaks by 3 dB at the input for all lengths. Equations (10-8) and (10-10) give designs with only small differences in gain.

The value of  $P$  controls one edge of the visible region. Setting  $P = 0$  centers the visible region about  $\psi = 0$ . End fire occurs at  $P = 1$ . As we increase  $P$  beyond 1, the beam peak of the distribution in  $\psi$  space moves into invisible space and the sidelobe level increases. A progression of the distribution sidelobes becomes beam peaks as  $P$  increases. Since the amplitude difference between sidelobes decreases as the sidelobe

number increases, the sidelobe level of the pattern increases as the pattern degrades because  $P$  exceeds the value given by Eq. (10-9).

Figure 10-1 shows the effects on directivity of varying  $P$  on an axisymmetrical traveling-wave antenna with a uniform amplitude distribution. For broadside radiation ( $P = 0$ ) and for  $P$  near end fire, the directivity is a constant value with scan:

$$\text{directivity} = \frac{2L}{\lambda} \quad (10-11)$$

When the broadside conical beam is scanned until the cone joins into a single end-fire beam, the directivity increases. For end fire,  $P = 1$ :

$$\text{directivity} = \frac{4L}{\lambda} \quad \text{end fire} \quad (10-12)$$

The directivity peaks for  $P$  given by Eq. (10-8):

$$\text{directivity} = \frac{SL}{\lambda} \quad (10-13)$$

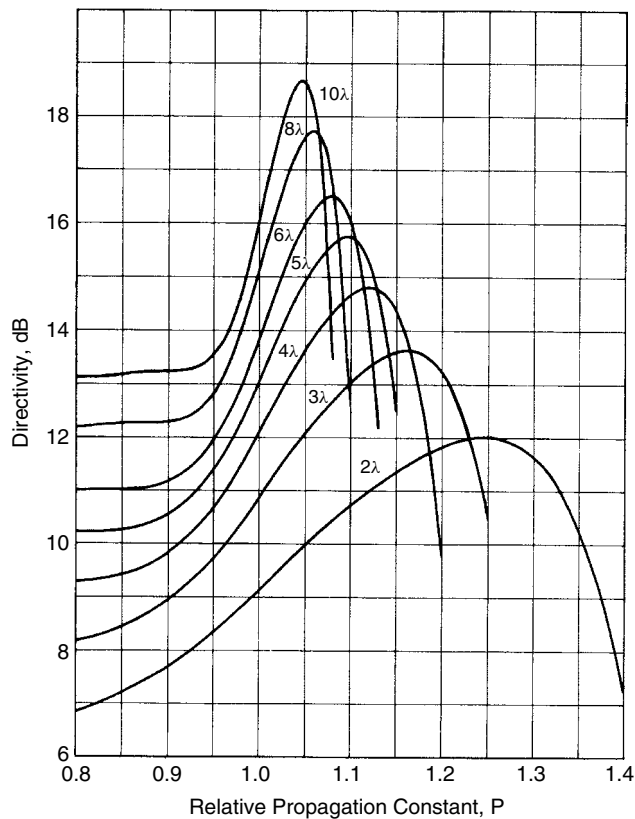


**FIGURE 10-1** Directivity of an axisymmetrical uniform-distribution traveling wave.

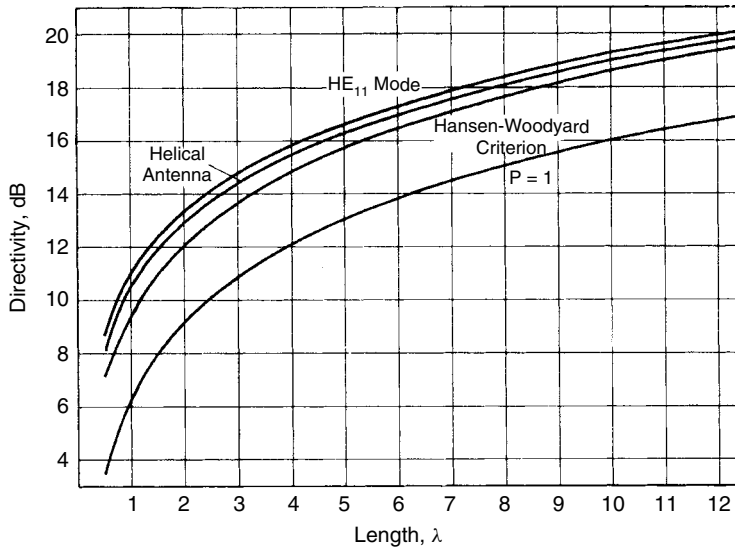


FIGURE 10-2 Directivity of an end-fire traveling-wave antenna.

$L/\lambda$	2	4	6	10	20
$S$	7.92	7.58	7.45	7.33	7.25

Figure 10-2 plots the maximum directivity of end-fire structures versus length. For the case  $P = 1$ , Eq. (10-12) gives the directivity on the curve. The Hansen and Woodward criterion increases the directivity as shown in Figure 10-2 for an infinitesimal-diameter structure. The distribution on the finite diameter of the helical wire antenna in the axial mode increases the directivity over that for the Hansen and Woodward increased directivity criterion. The hybrid mode with its linear polarization has a dipole null normal to the traveling-wave axis whose elemental pattern also increases directivity. Figure 10-3 is a plot of the corresponding beamwidths of those structures. Figure 10-2 sets an upper bound to the possible directivity of a small-diameter end-fire traveling-wave structure of given length.

### 10-1.1 Slow Wave

A slow wave exists on an open transmission-line structure that binds the wave by slowing a passing wave and bending it in the direction of the structure. In the same manner, a lens bends waves toward regions of higher index of refraction (increased slowing). We designate  $x$  as the direction normal to a planar structure and the radial coordinate  $\rho$  as the direction normal to the cylindrical slow-wave structure. The relation between propagation constants in various directions is found in any electromagnetics text [5]:

$$k_z^2 + k_x^2 = k^2 \quad \text{or} \quad k_z^2 + k_\rho^2 = k^2 \quad (10-14)$$

Since  $x$  (or  $\rho$ ) is unbounded, the waves must attenuate exponentially from the surface:

$$\alpha = jk_x \quad \text{or} \quad \alpha = jk_\rho \quad (10-15)$$

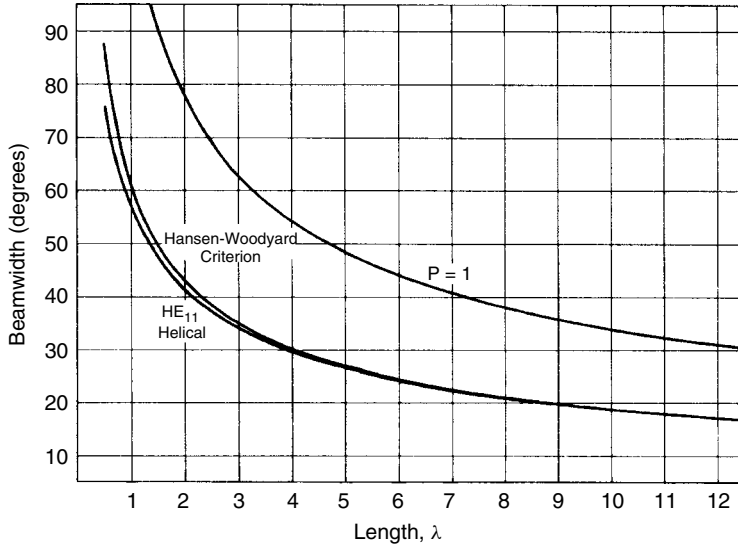


FIGURE 10-3 Beamwidth of a traveling-wave end-fire antenna.

The  $z$ -directed propagation constant becomes

$$k_z^2 = k^2 + \alpha^2 = P^2 k^2$$

where

$$P = \sqrt{1 + \frac{\alpha^2}{k^2}} = \sqrt{1 + \left(\frac{\lambda\alpha}{2\pi}\right)^2} \quad (10-16)$$

$P$ , the relative propagation constant, becomes a measure of the wave binding to the surface. We rearrange Eq. (10-16):

$$\alpha = \frac{2\pi}{\lambda} \sqrt{P^2 - 1} \text{ (Np}/\lambda) = 8.63 \frac{2\pi}{\lambda} \sqrt{P^2 - 1} \text{ (dB}/\lambda)$$

As  $P$  increases, the wave is more tightly bound to the surface. Figure 10-4 is a plot of the distances normal to the surface of constant-field contours versus  $P$ . The fields attenuate rapidly normal to the surface. For  $P \rightarrow 1$ , the slow-wave structure only diffracts passing plane waves without capturing the power. This is the sense of a cutoff frequency for the structure.

Most surface-wave antennas consist of three regions. The feed region launches the wave on the structure with  $P$  between 1.2 and 1.3 [4]. The structure tapers in a short section until  $P$  suitable for the length is reached. We design for a given phase shift along the entire length. For example, a long antenna would be designed so that the wave on the structure has an excess phase shift of  $180^\circ$  [Eq. (10-9)] over the traveling wave in free space. Near the end we sometimes taper the structure to reduce the end reflection given approximately by [4]  $P^2 - 1$  (power). This end taper can be quite short and achieve good results.

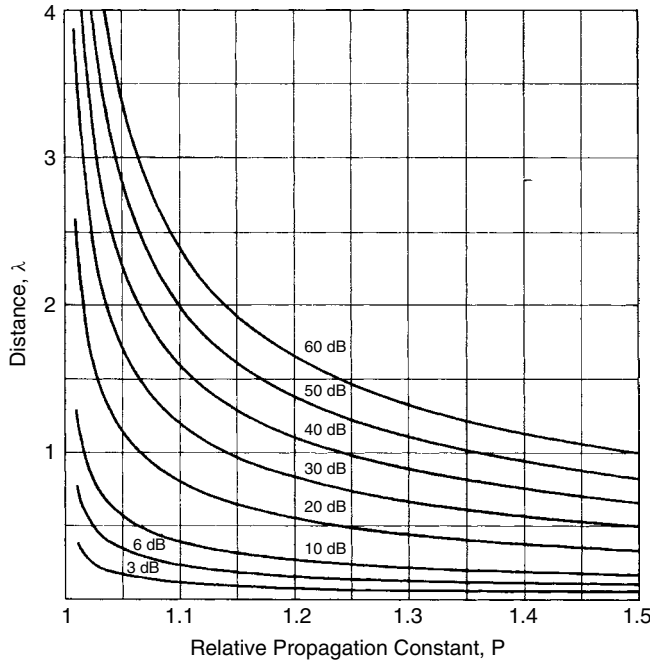


**FIGURE 10-4** Constant field contours off the surface of a surface-wave structure.

### 10-1.2 Fast Waves (Leaky Wave Structure)

Only closed structures such as waveguides support fast waves. An open structure requires a negative  $\alpha$  [Eq. (10-16)] for fast waves, which implies an exponentially increasing wave away from the structure. The structure soon radiates all its power and no longer guides the wave. By limiting  $\alpha$ , the leakage, we can extend the length of the radiating structure. We include the attenuation due to leakage in the  $z$ -axis propagation constant, in general, but we ignore it when  $\alpha$  is small:  $\theta_{\max} = \cos^{-1}(k_z/k)$ .

**Example** A rectangular waveguide has  $k_x = 2\pi/2a$  for the  $\text{TE}_{10}$  mode, where  $a$  is the guide width. We determine the  $z$ -directed propagation constant

$$k_z = \sqrt{k^2 - \left(\frac{\pi}{a}\right)^2}$$

which gives us

$$P = \sqrt{1 - \left(\frac{\lambda}{2a}\right)^2} = \cos \theta_{\max}$$

The waveguide propagation constant determines the direction of radiation from a traveling wave leaking out of the guide at a slow rate. We compute the guide width to give radiation in a given direction from

$$a = \frac{\lambda}{2\sqrt{1 - \cos^2 \theta_{\max}}}$$

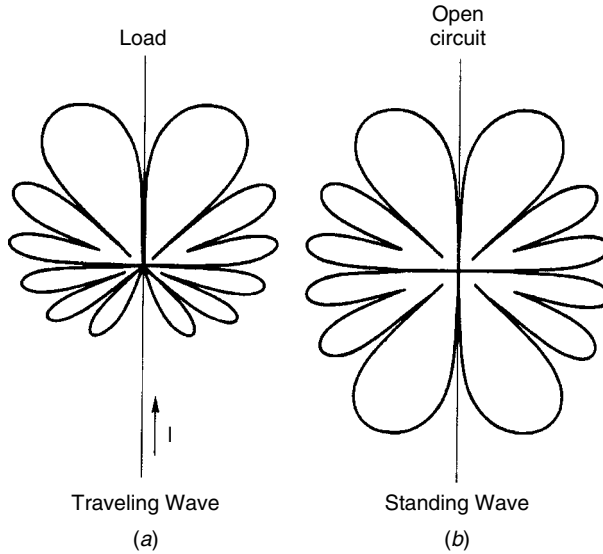


FIGURE 10-5 Patterns of long-wire antennas ( $3\lambda$  long): (a) traveling wave; (b) standing wave.

## 10-2 LONG WIRE ANTENNAS

One of the simplest traveling-wave antennas consists of a terminated wire. A standing wave can be divided into two waves traveling in opposite directions. By terminating the wire, we eliminate or reduce the reflected wave and its radiation. The uniform current traveling on a wire is given by  $I = I_0 e^{-jkPz}$ . We insert this current into Eq. (2-3) to compute the magnetic vector potential and use Eq. (2-1) to calculate the electric field. The resulting radiation intensity is

$$U = \frac{\eta |I_0|^2}{(2\pi)^2} \sin^2 \theta \left[ \frac{\sin[kL(p - \cos \theta)/2]}{P - \cos \theta} \right]^2 \quad (10-17)$$

Equation (10-17) separates into two pattern factors:  $\sin^2 \theta$ , the pattern of an incremental current element, and Eq. (10-6) for the uniform distribution. The null at  $\theta = 0$  due to the current element pushes the beam peak off the axis of the traveling wave. Figure 10-5 shows the patterns of traveling-wave and standing-wave currents using a 40-dB scale for  $L = 3\lambda$ . The patterns are axisymmetrical about the wire. Table 10-1 lists the beam peak direction and the directivity of the pattern for various lengths. The beam peak approaches the wire as the length increases. If we remove the termination, a wave reflects from the end and forms a beam in the opposite direction (Figure 10-5b). The small backlobes due to the forward-traveling wave have little effect on the main beam from the backward-traveling wave.

### 10-2.1 Beverage Antenna [6]

A Beverage antenna consists of a wire strung horizontally a fraction of a wavelength over ground (Figure 10-6). The antenna must be fed relative to ground, and its ground



TABLE 10-1 Characteristics of a Traveling-Wave Current on a Straight Wire

Length ( $\lambda$ )	Directivity (dB)	Beam Peak (deg)	Length ( $\lambda$ )	Directivity (dB)	Beam Peak (deg)
0.5	3.55	64.3	5.5	11.32	20.2
1.0	5.77	47.2	6.0	11.61	19.4
1.5	7.06	38.9	6.5	11.88	18.7
2.0	8.00	33.7	7.0	12.13	17.9
2.5	8.71	30.1	7.5	12.37	17.4
3.0	9.30	27.5	8.0	12.59	16.8
3.5	9.81	25.2	8.5	12.80	16.3
4.0	10.25	23.8	9.0	13.00	15.8
4.5	10.64	22.3	9.5	13.18	15.4
5.0	11.00	21.3	10.0	13.35	15.0

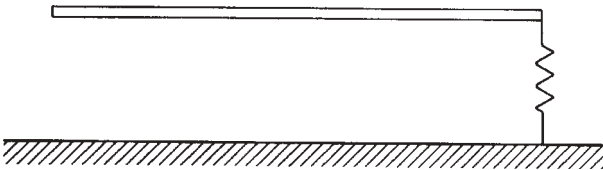


FIGURE 10-6 Beverage antenna.

plane image of the horizontally polarized wire cancels much of the far-field pattern of the antenna. Table 10-1 gives the length for a given takeoff angle for sky waves. The antenna can have good directivity but poor efficiency, since a great deal of the power is absorbed by the load.

We make a vertically polarized Beverage antenna by elevating the feed point on a tower and tilting the wire to the load on the ground. The beam due to the wire and its image add to form a horizontal beam when the wire tilt equals the beam direction given by Table 10-1 for a given length. The vertically polarized antenna needs a more conductive ground plane than the horizontally polarized antenna because soil reflects horizontally polarized waves better than vertically polarized waves. We may vary the tilt angle to produce a takeoff angle, but the beams of the wire and its image may no longer add. It is difficult to feed the tilted antenna because it is fed relative to ground at an elevated point.

10-2.2 V Antenna

We separate two Beverage antennas by an angle and feed from a balanced line to form a V antenna. When the separation angle is twice that given by Table 10-1, the beam peaks of the individual wires add. The balanced line input eases the feed problem of the Beverage antenna, since the antenna no longer feeds against ground. We place the input on a single insulating tower and stretch sloping wires to ground (Figure 10-7) to produce a beam. The beam is horizontal when the tilt angle equals the beam peak angle of Table 10-1. By varying the tilt angle, we change the elevation angle of the beam. A balanced feed produces horizontal polarization on the V antenna and reduces the requirement for a ground screen. The antenna impedance is about 800  $\Omega$ . The

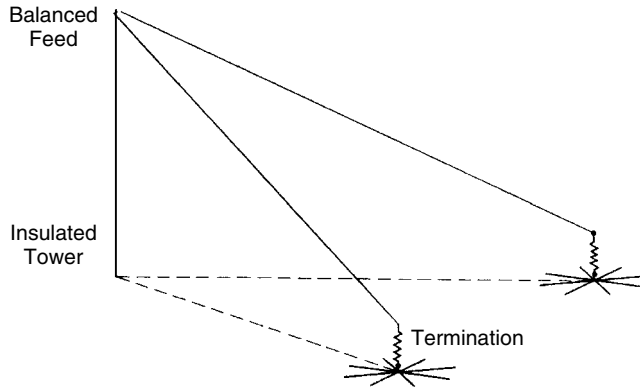


FIGURE 10-7 Sloping V antenna.

pattern contains high sidelobes with an overall low efficiency, but the bandwidth of the terminated antenna approaches an octave.

We can also make an unterminated V antenna. One method is to connect  $\lambda/4$  rods, which extend in the same direction as the V elements, to the normally grounded end of the loads on the V antenna [7]. The open-circuited quarter-wavelength lines reflect a short circuit to the loads over a limited bandwidth. The terminating resistors reduce the backlobe from that of the unterminated V antenna while eliminating the need for grounding the loads. In a second design a moment method solution is used to determine the angle between the elements to optimize the directivity of a beam halfway between the directions of the expanding elements [8]. The angle between the elements is fitted to a polynomial:

$$\alpha = -149.3 \left( \frac{L}{\lambda} \right)^3 + 603.4 \left( \frac{L}{\lambda} \right)^2 - 809.5 \frac{L}{\lambda} + 443.6 \text{ degrees} \quad \text{for } 0.5 \leq L/\lambda \leq 1.5$$

or

$$\alpha = 13.36 \left( \frac{L}{\lambda} \right)^2 - 78.27 \frac{L}{\lambda} + 169.77 \quad \text{for } 1.5 \leq L/\lambda \leq 3.0 \quad (10-18)$$

where  $L$  is the length of each arm. The maximum directivity at  $\alpha$  given by Eq. (10-18) is

$$\text{directivity} = 2.94 \frac{L}{\lambda} + 1.15 \quad \text{dB} \quad (10-19)$$

### 10-2.3 Rhombic Antenna [9]

The rhombic antenna consists of two V antennas. The second V antenna brings the two sides back together and makes it possible to connect the balanced lines to a single terminating resistor (Figure 10-8). Using a single terminating resistor eliminates the grounding problem of V-antenna terminations when the antenna transmits, although the load absorbs up to one-half of the transmitter power. Figure 10-8 shows the patterns of the individual wire radiators on the elements and the combined pattern in the horizontal

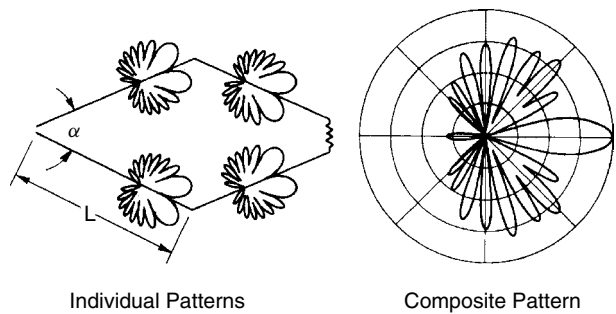


FIGURE 10-8 Rhombic antenna.

TABLE 10-2 V Angle  $\alpha$  for Maximum Output of a Rhombic Antenna Given the Elevation Angle

Arm Length, $L/\lambda$	Elevation Angle (deg)						
	0	5	10	15	20	25	30
1.5	90	89	88	86	84	80	76
2.0	77	76	75	73	70	66	60
2.5	69	68	66	64	60	56	48
3.0	62	61	60	57	52	48	40
3.5	58	57	55	52	47	42	34
4.0	54	53	50	47	42	36	28
4.5	51	50	47	43	38	32	24
5.0	48	47	44	40	35	28	20
6.0	44	43	40	36	30	22	14
7.0	41	38	36	32	25	18	8
8.0	38	37	34	28	22	14	
10.0	34	32	29	23	16		
15.0	28	26	22	15			
20.0	24	22	17				

Source: [9].

plane for the antenna in free space that unfortunately has high sidelobes. The peak pattern output occurs when the angle  $\alpha$  is approximately twice the peak radiation angle of the individual wires. Table 10-2 lists the angle  $\alpha$  for the maximum output for a given elevation angle when we mount the antenna parallel with ground. We raise the antenna a height  $H$  over ground to control its beam elevation angle:

$$H = \frac{\lambda n}{4 \sin \Delta} \quad n = 1, 3, 5, \dots \tag{10-20}$$

where  $\Delta$  is the elevation angle measured from the horizon and  $n$  is an odd integer. The elevated beam forms from a combination of the antenna and its ground image radiations. Because the antenna radiates horizontal polarization, the requirement for a ground-plane screen is minimal.

The terminating resistor should be about  $600\ \Omega$ , and the input impedance varies from 600 to  $900\ \Omega$  over an octave bandwidth, the actual value depending on frequency, height, and load resistor. We can use multiple wires that spread apart at the corners to reduce the impedance variation over the band and increase the power-handling capability of smaller wires. We build an inverted V antenna by mounting half a rhombic antenna over a ground plane. We use a single insulated tower; and by controlling the wire tilt angle with respect to ground, we combine the beams for the wire and its ground image into a horizontal beam. The inverted V places both the input and the terminating load on the ground. Because the antenna is vertically polarized, we must provide a good ground screen. In outdoor applications we ground and feed the antenna through a transformer to give some lightning protection and to match the high input impedance of the antenna.

### 10-3 YAGI–UDA ANTENNAS [10]

A Yagi–Uda antenna uses mutual coupling between standing-wave current elements to produce a traveling-wave unidirectional pattern. It uses parasitic elements around the feed element for reflectors and directors to produce an end-fire beam. Because the antenna can be described as a slow wave structure [11], the directivity of a traveling-wave antenna (Figure 10-2) is bounded when we include the directivity due to the element pattern. Maximum directivity depends on length along the beam direction and not on the number of elements.

Consider two broadside-coupled dipoles. We describe the circuit relation between them by a mutual impedance matrix:

$$\begin{bmatrix} V_1 \\ V_2 \end{bmatrix} = \begin{bmatrix} Z_{11} & Z_{12} \\ Z_{12} & Z_{22} \end{bmatrix} \begin{bmatrix} I_1 \\ I_2 \end{bmatrix} \quad (10-21)$$

where the diagonal elements of the matrix are equal from reciprocity. If we feed one element and load the other, we can solve for the input impedance of the feed antenna:

$$Z_{\text{in}} = \frac{V_1}{I_1} = Z_{11} - \frac{Z_{12}^2}{Z_{22} + Z_2} \quad (10-22)$$

where  $Z_2$  is the load on the second antenna. We short the second antenna ( $Z_2 = 0$ ) to maximize the induced standing-wave current and eliminate power dissipation:

$$Z_{\text{in}} = Z_{11} - \frac{Z_{12}^2}{Z_{22}} \quad (10-23)$$

The mutual impedance between broadside-coupled dipoles ( $Z_{12}$ ) approaches the self-impedance ( $Z_{11}$ ) as we move the dipoles close together and causes the input impedance [Eq. (10-23)] to approach zero.

The second equation of Eq. (10-21) for a shorted antenna relates the currents in the two dipoles:

$$0 = Z_{12}I_1 + Z_{22}I_2 \quad \text{or} \quad I_2 = -\frac{Z_{12}I_1}{Z_{22}} \quad (10-24)$$

Since  $Z_{12} \approx Z_{22}$ , the current in the shorted dipole is opposite the current in the feed element, and radiation from the induced current reduces the fields around the dipoles. Given the current on the parasitic element, we solve for the far field by array techniques. When the elements are spaced a distance  $d$ , with the parasitic element on the  $z$ -axis and the feed element at the origin, the normalized pattern response is

$$E = 1 + I_r e^{j(kd \cos \theta + \delta)}$$

where  $I_r e^{j\alpha} = I_2/I_1$  is the current of the parasitic element relative to the feed element. If we take the power pattern difference between the pattern at  $\theta = 0$  and  $\theta = 180^\circ$ , we get

$$|\Delta E|^2 = -2I_r \sin \delta \sin kd \quad (10-25)$$

*Case 1.*  $\delta = 180^\circ$ ,  $\Delta E = 0$ , and we have equal pattern levels in both directions with a null at  $\theta = 90^\circ$ .

*Case 2.*  $180^\circ < \delta < 360^\circ$ ,  $\Delta E > 0$ . The parasitic element is a director, and the pattern in its direction will be higher ( $\theta = 0$ ) than at  $\delta = 180^\circ$ .

*Case 3.*  $0^\circ < \delta < 180^\circ$ ,  $\Delta E < 0$ . The parasitic element is a reflector because the pattern away from it ( $\theta = 180^\circ$ ) is higher than at  $\theta = 0^\circ$ . We look at the phase of the relative currents to determine whether a parasitic element is a director or a reflector.

The mutual impedance between dipoles has been reduced to equations for a variety of configurations [12–16]. By use of these equations, Figure 10-9 was generated to show the phasing between a half-wavelength dipole and a parasitic dipole as the length and spacing are varied. A parasitic dipole of given length can be either a director or a reflector for different element spacing. Generally, a director is somewhat shorter and a reflector is somewhat longer than the feed element. If we reduce the length of the feed element or increase the element's diameter, the dividing line between a director and a reflector shifts upward. Figure 10-9 also shows the decreased element length at the transition point for additional spaced elements. Figure 10-10 illustrates a three-element Yagi–Uda dipole antenna having one reflector and one director around the feed element. The design is a compromise between various characteristics. With a 50- $\Omega$  source its response is as follows:

Gain = 7.6 dB	Front/back ratio = 18.6 dB
Input impedance = $33 - j7.5$	VSWR = 1.57 (50- $\Omega$ system)
$E$ -plane beamwidth = $64^\circ$	$H$ -plane beamwidth = $105^\circ$

With input matching we could increase the gain by 0.2 dB. A 3-dB gain bandwidth is 15% and a 1-dB gain bandwidth is 10%. At the 3-dB band edges the F/B ratio drops to 5.5 dB. As in many designs, the peak gain does not occur at the peak F/B value. The gain rises by 0.2 dB to a 50- $\Omega$  source at a point 3% higher in frequency than the point of maximum F/B. The maximum gain with input impedance matching (8.6 dB) occurs at a point 7% above the center frequency. The dipole element pattern narrows the  $E$ -plane beamwidth and produces a null at  $90^\circ$  from the boresight. The traveling wave alone forms the  $H$ -plane beam. A design to optimize the gain would have a phase progression along the elements to match Eq. (10-10) for short traveling-wave

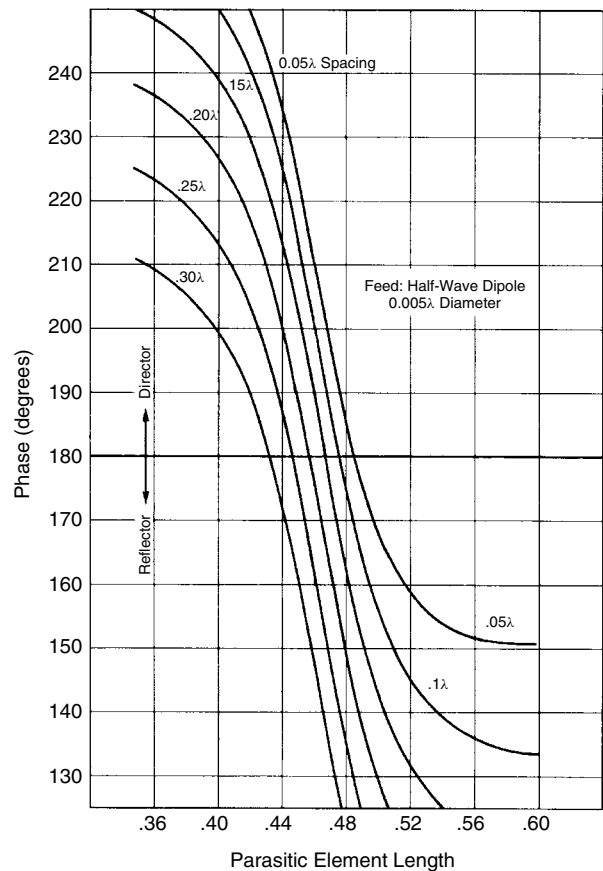


FIGURE 10-9 Phase of current on a parasitic dipole relative to current on a driven dipole.

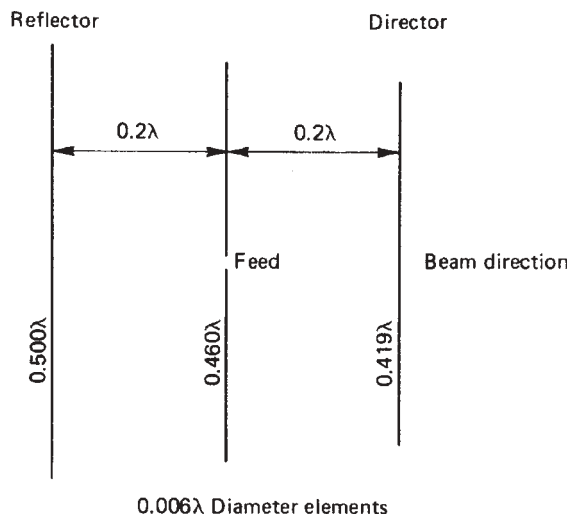


FIGURE 10-10 Three-element Yagi-Uda dipole antenna.

antennas. The array of dipoles samples an aperture  $0.6\lambda$  long. Figure 10-3 gives an  $H$ -plane beamwidth of about  $80^\circ$  for this optimum design. With only three elements we find difficulty in matching the phase distribution required and will produce a design with a low F/B value.

We analyze Yagi–Uda antennas by using the moment method [17]. First, calculate the mutual impedance matrix:

$$[V] = [Z][I] \quad (10-26)$$

The input voltage vector  $[V]$  has only one nonzero term (the feed). By solving the linear equations (10-26), we compute the currents at the base of each element. We assume a sinusoidal current distribution on each element [Eq. (5-1)] and solve for the pattern response from the array of dipoles. We calculate the input impedance of the array by using the moment method; and by retaining the current levels on the dipoles for a known input power, we can calculate gain directly.

The moment method allows reasonably quick calculation of the antenna characteristics so that optimization techniques can be applied. Cheng and Chen [18,19] use a perturbation technique that alternates between element spacings and lengths to find an optimum design with rapid convergence. Running a single iteration of each produces the design. No optimization technique can assure that a global optimum can be found. Designs will converge to local maximums. By limiting the search variables, the method of Cheng and Chen avoids some local optimums. Most optimizations work at a single frequency and produce designs with high gains that fall off rapidly with increasing frequency because the wave relative propagation constant increases with frequency. The gain curves in Figure 10-1 decrease rapidly after the peak point as the sidelobes increase. All traveling-wave end-fire antennas follow this pattern.

Kajfez [20] developed a method for optimizing over a band of frequencies. His method is to reduce the peak gain while increasing the bandwidth and reducing some of the tolerance requirements. We fix the band limits at frequencies  $f_1$  and  $f_2$  and optimize a composite cost function containing both the average directivity and the ripple or deviation from the average. Maximize

$$C = D_{\text{avg}} - wd \quad (10-27)$$

where  $D_{\text{avg}}$  is the average directivity and  $d$  is the RMS deviation of the directivity from  $D_{\text{avg}}$  over the band weighted by  $w$ :

$$D_{\text{avg}} = \frac{1}{f_2 - f_1} \int_{f_1}^{f_2} D(f) df$$

$$d = \sqrt{\frac{1}{f_2 - f_1} \int_{f_1}^{f_2} [D(f) - D_{\text{avg}}]^2 df} \quad (10-28)$$

$D(f)$  is the directivity function (a ratio, not dB). We vary  $w$  to stress either high directivity or design flatness. If  $w$  is made two or more times greater than the directivity expected, an optimization routine will design an antenna with a flat response. We calculate the integrals by using Gauss–Legendre quadrature, which requires only a few evaluations of the pattern response (five to eight).

We usually use only one reflector element. More elements can be used, but they add little. The gain of a two-element pair—a feed dipole and a reflector dipole—rises with increasing separation in a broad peak starting about  $0.15\lambda$ , peaking about  $0.20\lambda$ , and falling slowly with greater spacing. The reflector primarily affects F/B. As we move it closer to the feed element, the impedance level of the antenna drops. The response of the antenna is less sensitive to the diameter of the reflectors than to the director diameters, and it requires smaller adjustments to the length to compensate the design for the change.

We add length to the antenna to increase gain by adding director elements. Length along the axis, not the number of elements, produces gain provided that element currents are phased correctly. Beyond  $0.3\lambda$  to  $0.4\lambda$  spacings, the coupling drops and reduces control of the current phasing on the directors. Changing the diameters of directors requires changing the element lengths to retune the antenna. In one method, computer optimization routines are used to vary the dimensions to optimize some cost function. The lengths of the feed and first director elements have the greatest effect on gain. If we use a gradient-type search, we observe that most of the design concentrates on varying those element lengths. In long antennas with many directors the elements far from the feed change little from initial lengths by a gradient search. We can also adjust the lengths to match the current phasing of the elements to a distribution such as that given by Eq. (10-10). Manual tuning requires a retuning of the two elements closest to the feed and the feed element after tuning each director.

When adjusting the lengths to maximize bandwidth [Eqs. (10-27) and (10-28)], we should optimize gain to a given source impedance. We can optimize a single-frequency antenna to any reasonable impedance level and design a matching network, but broadband antennas may produce difficult matching network problems when we try to achieve design gain. A moment method gives us the peak gain to a conjugate matched source, but to compute gain to a given source impedance  $Z_s$ , we multiply the voltage gain by

$$\frac{2\sqrt{\operatorname{Re}(Z_I)\operatorname{Re}(Z_s)}}{|Z_I + Z_s|} \quad (10-29)$$

where  $Z_I$  is the antenna input impedance. Equation (10-29) allows optimizations to a given source impedance.

Table 10-3 gives the dimensions of an antenna designed by using Eqs. (10-27) and (10-28) for a maximum gain to a  $50\text{-}\Omega$  source [Eq. (10-29)]. The normalized frequency limits are 0.95 to 1.05, with a weighting  $w$  of 15 on the RMS deviation  $d$ .

**TABLE 10-3 Six-Element Yagi–Uda Dipole Antenna with  $0.01\lambda$ -Diameter Elements**

Element Type	Element Length ( $\lambda$ )	Location Along Boom ( $\lambda$ )
Reflector	0.484	0
Feed	0.480	0.250
Director	0.434	0.400
	0.432	0.550
	0.416	0.700
	0.400	0.850



**TABLE 10-4** Normalized Frequency Response of the Yagi–Uda Dipole Antenna of Table 10-3

Normalized Frequency	Gain, 50- $\Omega$ Source (dB)	Max Gain (dB)	F/B (dB)	Input Impedance ( $\Omega$ )	VSWR, 50- $\Omega$ Source
0.90	4.8	6.3	1.4	$29.6 - j45.2$	3.36
0.92	7.0	7.7	3.6	$32.5 - j30.8$	2.29
0.94	8.4	8.7	6.5	$39.3 - j19.6$	1.65
0.96	9.0	9.2	9.9	$42.7 - j13.2$	1.39
0.98	9.4	9.5	14.4	$39.5 - j7.6$	1.34
1.00	9.7	10.0	22.7	$31.2 + j2.8$	1.61
1.02	9.5	10.6	21.1	$22.0 + j19.8$	2.70
1.04	8.1	11.1	12.2	$15.2 + j42.5$	5.79
1.06	5.5	10.8	7.2	$12.9 + j69.1$	11.4
1.08	2.5	8.9	3.7	$16.0 + j97.2$	15.2

Table 10-4 lists the calculated response of the antenna. Like many designs, gain falls off more rapidly on the high-frequency end. In this case maximum gain actually occurs at maximum F/B. Pattern calculations of a uniform traveling-wave distribution, satisfying the Hansen and Woodyard criterion, gives peak F/B when it is an odd integer multiple of  $\lambda/4$ , of which Yagi–Uda antennas are one example.

Higher gains can be attained for six elements. Chen and Cheng [19] achieved 13.4 dB, but for a restricted bandwidth. We achieve bandwidth by limiting gain, and with each added element we can improve flatness at a higher gain level. Kajfez shows a nearly constant gain–bandwidth product for different designs. The gradient search method used in the design in Table 10-3 is sensitive to initial conditions and often converges to a local maximum and misses the global maximum, because it cannot escape a local optimum. A better design may be achieved by using a new starting point.

Table 10-5 lists the design of a 16-element Yagi–Uda dipole antenna. In this case the optimization routine manipulated elements 4 through 16 as a group to reduce the number of different-sized elements to four. This technique reduces tooling cost and causes little loss in possible performance. Since the size of the last few directors has only a minor effect on the total gain, most of the iterations in an optimization routine are spent changing the elements around the driven dipole and only slowly changing those elements. We adjust the reflector, feed element, and first director to match into the uniform surface wave structure of equally spaced elements.

**TABLE 10-5** Sixteen-Element Yagi–Uda Dipole Antenna with  $0.006\lambda$ -Diameter Elements

Element	Element Length ( $\lambda$ )	Element Spacing ( $\lambda$ )
Reflector	0.4836	0.2628
Feed	0.4630	0.2188
Director 1	0.4448	0.2390
Directors 2 to 13	0.4228	0.2838

The frequency response (Table 10-6) has a peak gain equal to the value given by Figure 10-2 for the hybrid mode and at this overall length. Like many Yagi-Uda dipole antennas, this antenna matches best to a low input impedance ( $30\ \Omega$ ). The gain rises slowly below the resonant frequency of the antenna and falls rapidly for higher frequencies, as predicted by Figure 10-1, which shows gain versus relative propagation constant along a uniform surface-wave structure.

The element diameter affects the optimum length of the Yagi-Uda dipole elements. A number of optimum Yagi-Uda dipole antennas of various overall lengths were built with different-diameter elements and adjusted to regain optimum performance [21]. Table 10-7 summarizes the length changes required of directors when their diameters are changed. Similarly, Table 10-8 lists the changes required for reflectors. Tables 10-7 and 10-8 require little or no change in the feeder element length to regain the optimum design. We use the tables to modify element lengths when changing

**TABLE 10-6 Normalized Frequency Response of a 16-Element Yagi-Uda Dipole Antenna**

Normalized Frequency	Gain, 30- $\Omega$ Source (dB)	F/B (dB)	Input Impedance ( $\Omega$ )	VSWR, 30- $\Omega$ Source
0.95	12.1	12.2	$26.7 - j36.1$	3.34
0.96	13.4	12.2	$28.4 - j26.4$	2.40
0.97	14.4	12.2	$31.6 - j17.7$	1.77
0.98	15.0	13.3	$34.3 - j12.1$	1.49
0.99	15.5	17.3	$32.2 - j7.3$	1.28
1.00	15.9	35.1	$27.0 + j3.4$	1.17
1.01	15.2	15.6	$27.3 + j20.8$	2.05
1.02	14.0	10.6	$40.4 + j33.0$	2.61
1.03	13.7	11.8	$36.0 + j23.5$	2.06
1.04	8.2	16.4	$22.8 + j51.5$	5.77
1.05	5.4	4.7	$54.1 + j68.2$	5.03

**TABLE 10-7 Length Changes of Directors in a Yagi-Uda Dipole Antenna for Various Diameters**

Dipole Diameter ( $\lambda$ )	Dipole Length Change ( $\lambda$ )	Dipole Diameter ( $\lambda$ )	Dipole Length Change ( $\lambda$ )
0.001	0.030	0.008	0.006
0.0012	0.029	0.009	0.002
0.0015	0.027	0.010	0.000
0.002	0.025	0.012	-0.004
0.0025	0.023	0.015	-0.010
0.003	0.021	0.020	-0.018
0.004	0.017	0.025	-0.024
0.005	0.014	0.030	-0.029
0.006	0.011	0.040	-0.038
0.007	0.008		

Source: [21].

**TABLE 10-8 Length Changes of Reflectors in a Yagi–Uda Dipole Antenna for Various Diameters**

Dipole Diameter ( $\lambda$ )	Dipole Length Change ( $\lambda$ )	Dipole Diameter ( $\lambda$ )	Dipole Length Change ( $\lambda$ )
0.001	0.011	0.008	0.002
0.002	0.008	0.010	0.000
0.003	0.006	0.020	−0.003
0.004	0.005	0.030	−0.005
0.006	0.003	0.040	−0.006

Source: [21].

**TABLE 10-9 Length Changes to Increase Elements of a Yagi–Uda Dipole Antenna to Account for Boom Diameter**

Boom Diameter ( $\lambda$ )	Dipole Length Change ( $\lambda$ )	Boom Diameter ( $\lambda$ )	Dipole Length Change ( $\lambda$ )
0.002	0.0010	0.022	0.0158
0.004	0.0022	0.024	0.0173
0.006	0.0034	0.026	0.0189
0.008	0.0048	0.028	0.0205
0.010	0.0064	0.030	0.0220
0.012	0.0084	0.032	0.0236
0.014	0.0095	0.034	0.0252
0.016	0.0111	0.036	0.0265
0.018	0.0127	0.038	0.0283
0.020	0.0142	0.040	0.0299

Source: [21].

diameters. Element length tolerance is  $0.003\lambda$ . The boom supporting the elements also affects element length for optimum designs. Table 10-9 lists element length increase versus boom diameter.

**Example** Determine the length adjustment necessary when building the design of Table 10-5 with  $0.002\lambda$  elements.

From Table 10-7, the length adjustment for  $0.006\lambda$  is  $0.010\lambda$  and the adjustment for  $0.002\lambda$ -diameter elements is  $0.025\lambda$ . We increase the lengths of the directors by the difference,  $0.015\lambda$ . Similarly, from Table 10-8 we increase the reflector length by  $0.005\lambda$ . For a boom diameter of  $0.02\lambda$  we also increase the lengths of all the elements by  $0.0142\lambda$  (Table 10-9).

### 10-3.1 Multiple-Feed Yagi–Uda Antennas

We further improve the response of Yagi–Uda antennas by directly feeding more than one element. The convenience of Yagi–Uda antennas lies in the single feed point. With many feed points a log-periodic dipole antenna (Section 11-12) produces a wider band design. Figure 10-11 illustrates a four-element design with a crisscross feeder. Table 10-10 lists the calculated response of the antenna. The gain response is flat with good F/B and input VSWR over the band for this short antenna ( $0.3\lambda$  long), where

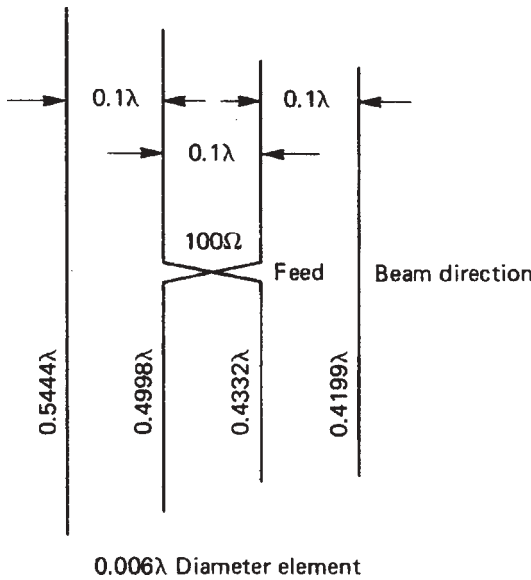


FIGURE 10-11 Multiple-feed Yagi-Uda dipole antenna.

TABLE 10-10 Normalized Frequency Response of a Four-Element Yagi-Uda Dipole Antenna with a Crisscross Feeder Between Two Elements (Figure 10-11)

Normalized Frequency	Gain, 50-Ω Source (dB)	F/B (dB)	Input Impedance (Ω)	VSWR, 50-Ω Source
0.90	7.0	12.1	$30.1 + j14.0$	1.82
0.92	7.1	17.5	$42.6 + j4.0$	1.20
0.94	7.0	21.9	$44.0 - j3.0$	1.15
0.96	6.9	25.9	$43.9 - j5.8$	1.20
0.98	7.0	31.3	$44.4 - j7.3$	1.22
1.00	7.0	53.0	$45.2 - j9.4$	1.25
1.02	7.1	30.7	$44.8 - j13.5$	1.35
1.04	7.2	23.6	$40.0 - j18.8$	1.60
1.06	7.0	19.0	$29.0 - j20.5$	2.12
1.08	6.5	15.3	$16.5 - j14.2$	3.29
1.10	5.0	11.9	$8.0 - j2.3$	6.30

the crisscross feeder adds an additional 180° phase shift along the length to produce a backfire pattern from a fast wave.

The simple antenna of Figure 10-12 uses only two dipole elements with a crisscross feed. Like many Yagi-Uda dipole antennas, this antenna, matches best to a low-impedance (25-Ω) source. Although its gain and bandwidth (Table 10-11) are less than those of the four-element multiple-feed antenna, its bandwidth is better than that of a singly fed equivalent antenna. The length along the boom still determines the ultimate gain of the antenna, but the backfire crisscross feed improves F/B.

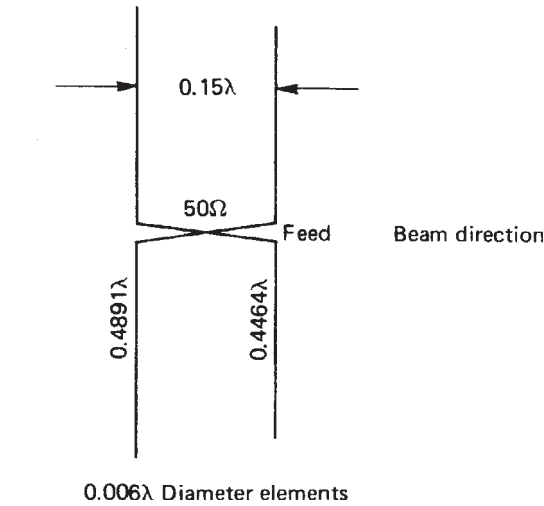


FIGURE 10-12 Dipole two-element backfire antenna.

TABLE 10-11 Normalized Frequency Response of a Two-Element Crisscross-Fed Antenna

Normalized Frequency	Gain (dB), 25-Ω Source	F/B (dB)	Input Impedance (Ω)	VSWR, 25-Ω Source
0.95	5.0	13.1	$12.8 - j1.6$	1.96
0.96	5.2	14.8	$13.6 - j0.5$	1.84
0.97	5.4	17.0	$14.4 + j0.8$	1.74
0.98	5.6	20.0	$15.2 + j2.3$	1.67
0.99	5.8	24.6	$16.0 + j3.9$	1.62
1.00	5.9	34.1	$17.0 + j5.9$	1.61
1.01	6.0	29.0	$18.2 + j8.2$	1.64
1.02	6.1	22.0	$19.7 + j10.8$	1.71
1.03	6.1	18.1	$21.7 + j14.0$	1.84
1.04	6.1	15.3	$24.3 + j17.6$	2.02
1.05	6.1	13.2	$27.9 + j22.0$	2.36

We can no longer just use Eq. (10-26), the matrix equation of mutual impedances, to analyze a multiple-feed antenna. We invert the mutual impedance matrix and add a  $2 \times 2$  admittance matrix of the transmission-line feeders between the dipole center point nodes:

$$[I] = [Y_a + Y_f][V] \tag{10-30}$$

where  $Y_a$  is the dipole mutual admittance matrix and  $Y_f$  is the feeder admittance matrix. Since most of the elements are short-circuited, we reduce the matrix [Eq. (10-30)] to only the terms involving unshorted dipoles and solve for the input voltages for a current vector with one nonzero term (the input). We return to Eq. (10-26) and use the voltage vector obtained from the solution of Eq. (10-30) to calculate dipole base currents.

Multiple feeds can also be used to reduce sidelobes. A backward-wave excited array (crisscross feeder) feeding a Yagi–Uda dipole antenna reduced the antenna sidelobes [22]. The extra feed points add degrees of freedom for a part of design independent of the number of elements.

### 10-3.2 Resonant Loop Yagi–Uda Antennas

We can make Yagi–Uda arrays by using the resonant loop element (Section 5-18). The loop radiates its maximum signal normal to the plane of the loop (along the axis) and has a linearly polarized wave in the direction of the voltage across the feed. A two-element loop parasitic array, reported in 1942, was built to eliminate corona problems at high altitudes in Ecuador [23]. The maximum standing-wave voltage points occur at  $\lambda/4$  from the feed along the loop and not at the ends of rods, where air breakdown can occur. The symmetry of the loop reduces the effects of nearby structures on the antenna and they can be mounted at the voltage null opposite the feed, along a metal rod in a coaxial array with little effect.

Loop shape has only a minor effect on input impedance at a resonant perimeter length of about  $1.1\lambda$ . The larger size (and gain) of the basic element raises the gain of a parasitic (Yagi–Uda) array from an array made with dipoles. A simple antenna consists of two square loops (Figure 10-13) with a feed element and a parasitic reflector. The reflector perimeter is somewhat larger than the feed loop. Such an antenna, commonly called a *cubic quad*, is usually made by stretching wires on a frame. The direction of the voltage across the feed point determines the linear polarization sense. The antenna of Figure 10-13 radiates horizontal polarization as fed.

Table 10-12 lists the dimensions of antennas designed to be resonant (zero reactance) and have maximum F/B ratios with a wire radius of  $0.0002\lambda$ . The maximum F/B occurs for a loop spacing of  $0.163\lambda$ . Table 10-13 lists the frequency response of the antenna spaced at  $0.15\lambda$ . As with a Yagi–Uda dipole antenna, the design must be adjusted as the wire radius changes to obtain the same response. Table 10-14 lists the design changes on a logarithmic scale. The greater change occurs to the reflector perimeter.

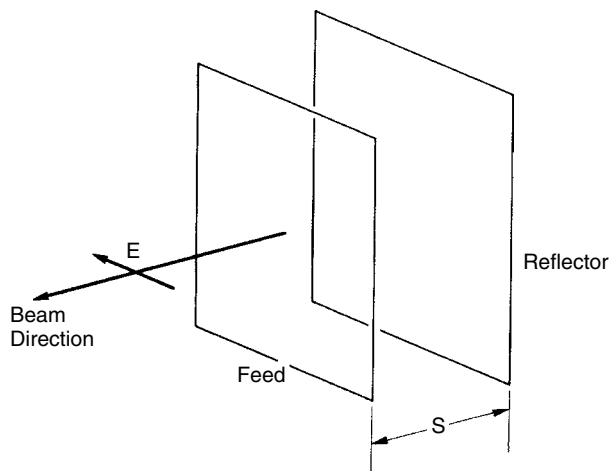


FIGURE 10-13 Cubic-quad traveling-wave resonant loop antenna.

**TABLE 10-12 Characteristics of Resonant Cubic-Quad Antennas,  $0.0002\lambda$ -Diameter Wire**

Element Spacing ( $\lambda$ )	Feed Perimeter ( $\lambda$ )	Reflector Perimeter ( $\lambda$ )	Gain (dB)	F/B (dB)	Input Resistance
0.10	1.000	1.059	7.2	17.5	76
0.15	1.010	1.073	7.1	32.8	128
0.16	1.013	1.075	7.1	46.1	137
0.163	1.014	1.0757	7.1	59.6	140
0.17	1.016	1.077	7.1	38.1	145
0.18	1.018	1.079	7.0	31.0	153
0.20	1.025	1.082	6.9	24.6	166

**TABLE 10-13 Normalized Frequency Response of a Cubic-Quad Antenna Resonant at a Spacing of  $0.15\lambda$** 

Normalized Frequency	Gain (dB)	F/B (dB)	Input Impedance ( $\Omega$ )
0.96	7.3	2.9	$38.5 - j140.9$
0.98	7.8	11.0	$72.9 - j55.4$
0.99	7.5	17.9	$100.5 - j22.4$
1.00	7.1	32.8	128.0
1.01	6.8	19.9	$150.7 + j13.3$
1.02	6.8	14.8	$167.0 + j24.2$
1.03	6.2	12.1	$178.0 + j35.1$
1.04	6.0	10.4	$185.4 + j47.3$
1.06	5.7	8.2	$195.0 + j77$
1.08	5.5	6.8	$202.0 + j113.4$

**TABLE 10-14 Cubic-Quad Antenna Adjustments for Changing Wire Diameter**

Wire Diameter ( $\lambda$ )	Reflector Perimeter ( $\lambda$ )	Feeder Perimeter ( $\lambda$ )
0.00005	-0.013	-0.002
0.0001	-0.007	-0.001
0.0002	0	0
0.0004	0.009	0.002
0.0008	0.019	0.003
0.0016	0.033	0.005
0.0032	0.052	0.008

When close to the final design, we adjust the reflector for maximum F/B and the feed loop for resonance independently. Each has little effect on the other.

We approach the design of coaxial loop arrays from traveling-wave phasing. Table 10-15 lists the traveling-wave relative propagation constant along an infinite array of loops. For a given array length we use Eq. (10-8) or (10-10) to determine the required mode relative propagation constant to maximize gain.

**TABLE 10-15 Relative Propagation Constant Along a Coaxial Array of Circular Loops**

Circumference, $2\pi b/\lambda$	$S/b$		
	0.25	0.50	1.00
0.74	1.05	1.03	1.01
0.76	1.06	1.04	1.016
0.78	1.08	1.05	1.02
0.80	1.09	1.06	1.03
0.82	1.12	1.08	1.04
0.84	1.14	1.11	1.06
0.86	1.17	1.13	1.07
0.88	1.20	1.16	1.09
0.90	1.24	1.20	1.12
0.92	1.30	1.26	1.16
0.94	1.37	1.32	1.23
0.96	1.47	1.40	1.32
0.98	1.60	1.55	1.44

Source: [24].

**Example** Compute the loop size for an array  $2\lambda$  long with the ratio of loop spacing to loop radius = 0.5 for maximum gain.

We use Eq. (10-10) with  $R = 4.5$  to calculate  $P = 1 + 1/9 = 1.111$ . By using Table 10-15, we have  $2\pi b/\lambda = 0.84$  and  $b = 0.134\lambda$ . The spacing between loops is  $0.5(0.134) = 0.0668\lambda$ , and 30 loops are required for an antenna length of  $2\lambda$ .

Table 10-15 suggests closely spaced elements. With further tabular data [25], designs with loop spacing up to  $0.3\lambda$  are possible. The reflector element is spaced  $0.1\lambda$  away from the exciter with a perimeter of  $1.05\lambda$  and we adjust the perimeter of the feed element to resonate the antenna.

In the design above, the Hansen–Woodyard criterion for maximum gain for the relative propagation constant was not used. The gain in Figure 10-1 falls rapidly for an increase in  $P$  (increased frequency), and we obtain a better pattern bandwidth by designing with less than the maximum gain value of  $P$ . The possible gain bandwidth shrinks (Figure 10-1) when we increase length to obtain more gain. This is a general property of all traveling-wave end-fire structures. Similarly, the beam of a leaky wave antenna ( $P < 1$ ) scans toward end fire with increasing frequency because  $P$  increases.

We can combine loops and dipoles in the same array. In some designs, dipoles are used for far-out directors in front of loops. Similarly, a parasitic loop can provide an effective reflector element for a dipole or crossed dipoles. A loop spaced  $0.25\lambda$  from a resonant dipole ( $0.47\lambda$  long) increased gain to 5.9 dB with an F/B value of 21.7 dB for a loop circumference of  $1.15\lambda$ .

#### 10-4 CORRUGATED ROD (CIGAR) ANTENNA

A corrugated rod traveling-wave structure consists of disks attached to a central metal rod (Figure 10-14). The rod supports a TM axisymmetrical mode with readily calculable parameters [2] that has a pattern null on axis. The hybrid mode  $HE_{11}$  (Section 7-3)



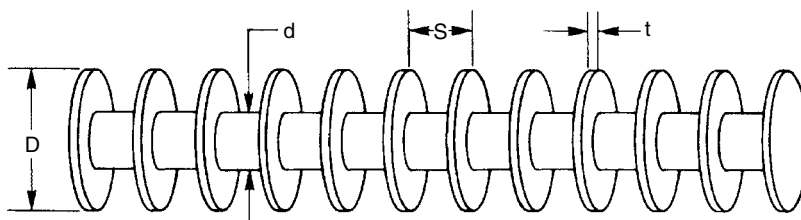


**FIGURE 10-14** Corrugated rod (cigar) traveling-wave structure.

**TABLE 10-16** Measured Relative Propagation Constant on a Corrugated Rod (Cigar) Antenna<sup>a</sup>

$(D - d)/\lambda$	$P$	$(D - d)/\lambda$	$P$
0.15	1.03	0.275	1.23
0.175	1.05	0.30	1.31
0.20	1.08	0.325	1.47
0.225	1.12	0.35	1.67
0.25	1.16	0.375	1.92

Source: [26].

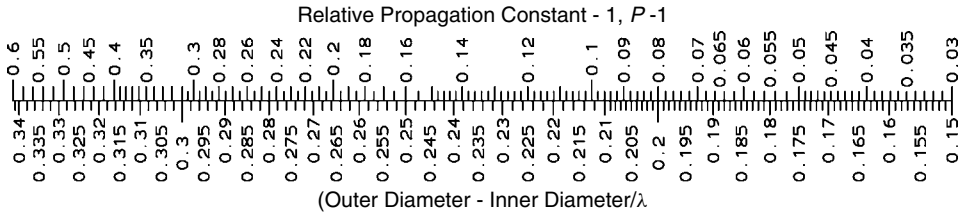
<sup>a</sup> $0.15 \leq \text{disk spacing}/\lambda \leq 0.21$ ;  $0.15 \leq \text{central rod diameter}/\lambda \leq 0.21$ ;  $0.018 \leq \text{disk thickness}/\lambda \leq 0.025$ .

propagates on the rod to produce a pattern with its peak on the axis with linear polarization. The hybrid mode is the sum of the  $\text{TE}_{11}$  and  $\text{TM}_{11}$  modes, and the surface wave has exponentially decaying radial fields.

We design this antenna empirically by measuring phase velocities along an excited structure. The gain increases slightly for an increased diameter, but it is determined primarily by length. Table 10-16 lists measured data for the range of disk spacing from  $0.15\lambda$  to  $0.21\lambda$ . In this range, disk spacing has a negligible effect on the wave velocity. We use this table with a given length to determine the necessary relative propagation constant  $P$ .

We can excite the corrugated rod from a number of feeding structures. A circular waveguide propagating the  $\text{TE}_{11}$  mode will excite the rod in the hybrid  $\text{HE}_{11}$  mode [26] when tapered into the guide. A resonant ring will excite the rod when backed by a suitable reflector ring or disk. Wong and King [27] excite the rod from an open-sleeve dipole in a cavity (Figure 5-28). The length of the rod controls the pattern beamwidth, and the feed structure controls the impedance. Each may be adjusted somewhat separately.

The traveling-wave disk on rod radiates high sidelobes of about 10 dB, which can be reduced by placing the antenna in a cone [27]. The rod runs the length of the cone and extends beyond the end by about  $0.72\lambda$ . This antenna uses a corrugated rod  $3.39\lambda$  long at the center frequency and is placed in a cone with a  $2.94\lambda$  diameter and a height of  $2.58\lambda$ . The rod was under the limit given above with a diameter of  $0.074\lambda$  and average disk diameter of  $0.311\lambda$ . Using the scale, we read  $P = 1.139$ , close to the optimum value of 1.137 for the given rod length. A disk spacing of  $0.24\lambda$  shows that we can build successful antennas beyond the limits given above and that the scale



**SCALE 10-1** Corrugated rod relative propagation constant  $P$  given dimensions.

can still be used. When placed in the cone, the sidelobes dropped to about  $-30$  dB, and when fed by the disk sleeve dipole shown in Figure 5-28, the antenna has a 34% 2:1 VSWR bandwidth. At a peak gain of 16.5 dB, the antenna exceeds the gain of a traveling-wave antenna by about 1 dB for its given length, but falls short of the gain of a horn by about 1 dB. Table 10-16 was interpolated to produce Scale 10-1 for the design of a corrugated rod.

**Example** Design a corrugated rod  $4\lambda$  long at 10 GHz (30 mm wavelength).

By using Eq. (10-13), we compute directivity  $= 7.58(4) = 30.32$  or 14.8 dB for  $P$  given by Eq. (10-8).  $P = 1 + 0.465/4 = 1.116$ . We use  $P - 1$  with Scale 10-1 to determine the difference between the central rod diameter and the disk diameter:  $(D - d)/\lambda = 0.2224$ . If we select the midpoint in the range of values for the dimensions, we obtain the dimensions of the corrugated rod in the center constant-dimension region. The disk spacing  $S = 0.18\lambda = 5.4$  mm. The central rod diameter  $d = 0.18\lambda = 5.4$  mm. The outer disk diameter  $D = 0.2224\lambda + 0.18\lambda = 0.4024\lambda = 12.07$  mm. The disk thickness  $t = 0.022\lambda = 0.66$  mm. The corrugated rod should start with  $P = 1.3$  at the feed point. We read  $(D - d)/\lambda = 0.2973$ , which calculates to an outer disk diameter  $D = (0.2973 + 0.18)\lambda = 14.32$  mm. The initial taper can be three disk elements long. At the end it is a good idea to taper the last few disk diameters to reduce end reflection.

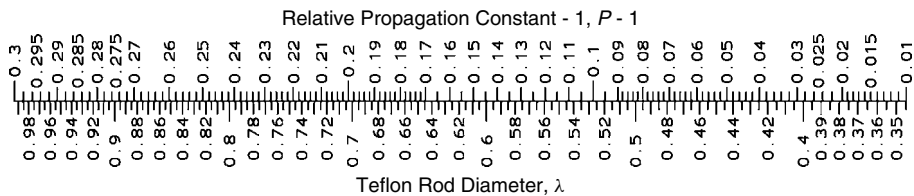
## 10-5 DIELECTRIC ROD (POLYROD) ANTENNA

A dielectric rod will support an  $HE_{11}$  hybrid mode. Inside the rod we describe the fields with Bessel function  $J_n$ . Outside the rod the fields fall off exponentially and we use the modified Bessel function  $K_n$ . The hybrid mode consists of the sum of  $TE_{11}$  and  $TM_{11}$  modes. To determine the mode velocity, we equate the propagation constants of the internal and external waves. This equation contains two constants and we eliminate one by equating the radially directed wave impedance at the boundary. The result is a transcendental equation that must be solved by graphical or numerical methods [2]. Table 10-17 summarizes the results of these calculations for common dielectrics. Interpolation of the table produces Scales 10-2 and 10-3 for design using Teflon or Delrin with a dielectric constant of 3.1.

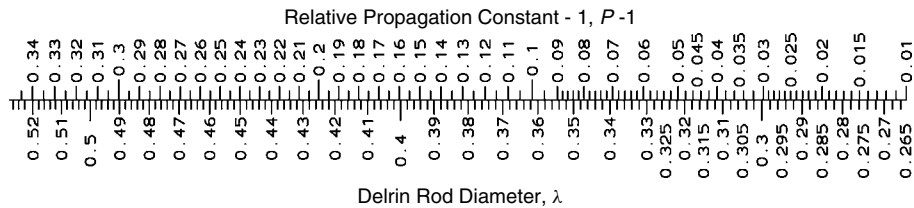
Figure 10-15 shows a common feeding arrangement for the polyrod antenna. The rod protrudes from a circular waveguide supporting the  $TE_{11}$  mode, which excites the hybrid mode  $HE_{11}$  on the rod. At the waveguide exit we use a rod diameter to give  $P$  from 1.2 to 1.3 so that the wave will be closely bound to the rod. The feeding

TABLE 10-17 Diameter of a Dielectric Rod Supporting an HE<sub>11</sub> Mode ( $\lambda$ )

<i>P</i>	Dielectric Constant				
	2.08	2.32	2.55	3.78	10
1.01	0.345	0.316	0.296	0.240	
1.02	0.378	0.345	0.322	0.257	0.1780
1.03	0.403	0.366	0.340	0.270	0.1824
1.04	0.425	0.384	0.356	0.279	0.1860
1.05	0.444	0.400	0.369	0.287	0.1888
1.06	0.462	0.414	0.381	0.294	0.1912
1.07	0.479	0.427	0.393	0.300	0.1933
1.08	0.495	0.440	0.404	0.306	0.1951
1.10	0.527	0.465	0.424	0.317	0.1983
1.12	0.559	0.489	0.444	0.327	0.2010
1.14	0.592	0.513	0.463	0.336	0.2034
1.16	0.627	0.538	0.482	0.344	0.2055
1.18	0.663	0.563	0.501	0.353	0.2074
1.20	0.703	0.590	0.521	0.361	0.2092
1.25	0.823	0.664	0.575	0.381	0.2133
1.30	0.994	0.758	0.638	0.402	0.2170
1.35	1.283	0.885	0.716	0.424	0.2205
1.40		1.081	0.820	0.448	0.2238



SCALE 10-2 Teflon rod HE<sub>11</sub>-mode relative propagation constant.



SCALE 10-3 Delrin rod HE<sub>11</sub>-mode relative propagation constant.

guide (Figure 10-15) has a quarter-wavelength choke to reduce the backfire lobe due to direct radiation from the transition [28]. The choke region can also be flared in a short horn [29].

The second region of the rod tapers either to a uniform diameter section to produce maximum gain or to a tapered section to reduce sidelobes. At the end of the antenna we taper the rod rapidly in a terminating section to bring the relative propagation constant

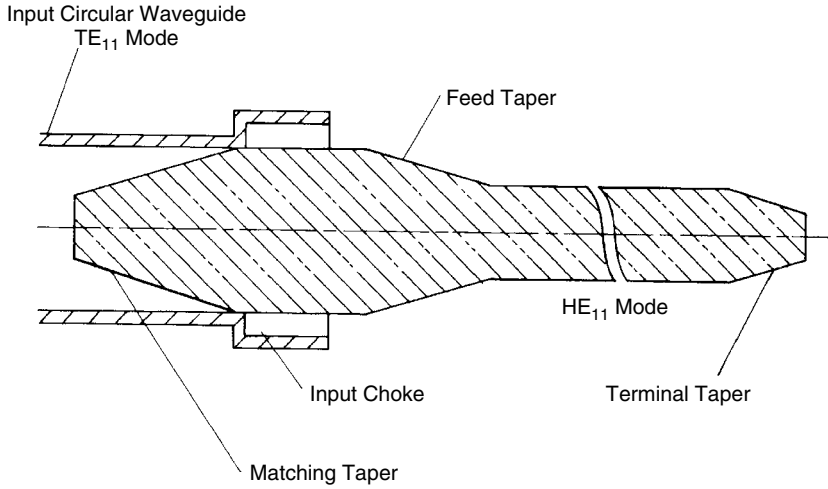


**FIGURE 10-15** Dielectric rod (polyrod) antenna.

of the surface wave near 1, to reduce reflection from the end. We calculate  $P$  along the guide and adjust the uniform section diameter or tapered section length to satisfy the total extra phase shift condition for maximum end-fire radiation.

**Example** Design a dielectric rod antenna  $5\lambda$  long using Teflon and compare it to a design using Delrin.

The relative propagation constant for peak gain is independent of the material, which we compute from Eq. (10-8):  $P = 1 + 0.465/5 = 1.093$ . By using Scales 10-2 and 10-3, we read the rod diameters:  $0.516\lambda$  for Teflon and  $0.356\lambda$  for Delrin. At the point where the rod exits from the feeding waveguide, a suitable relative propagation constant is 1.25. We use the scales to find the rod diameters:  $0.822\lambda$  for Teflon and  $0.456\lambda$  for Delrin. These diameters are proportional to the free-space wavelength, not the wavelength in the rod.

The loss tangent for Delrin is 0.005, whereas Teflon is only 0.0012; we need to consider the loss in the antenna. The loss for a wave propagating through a dielectric is given by

$$\frac{20\pi\sqrt{\epsilon_r}\tan\delta}{\lambda\ln 10} = \frac{27.3\sqrt{\epsilon_r}\tan\delta}{\lambda} \quad \text{dB}/\lambda$$

Consider that only a portion of the power in the wave propagates in the dielectric. We use the effective dielectric constant to determine a filling factor that reduces the loss:

$$\text{filling factor} = \text{QF} = \frac{1 - 1/\epsilon_{\text{eff}}}{1 - 1/\epsilon_r}$$

We relate the effective dielectric constant to  $P$ :  $\epsilon_{\text{eff}} = P^2 = (1.093)^2 = 1.195$ :

$$\text{loss(dB)} = 27.3\text{QF}\sqrt{\epsilon_r}\tan\delta[\text{Length}(\lambda)]$$

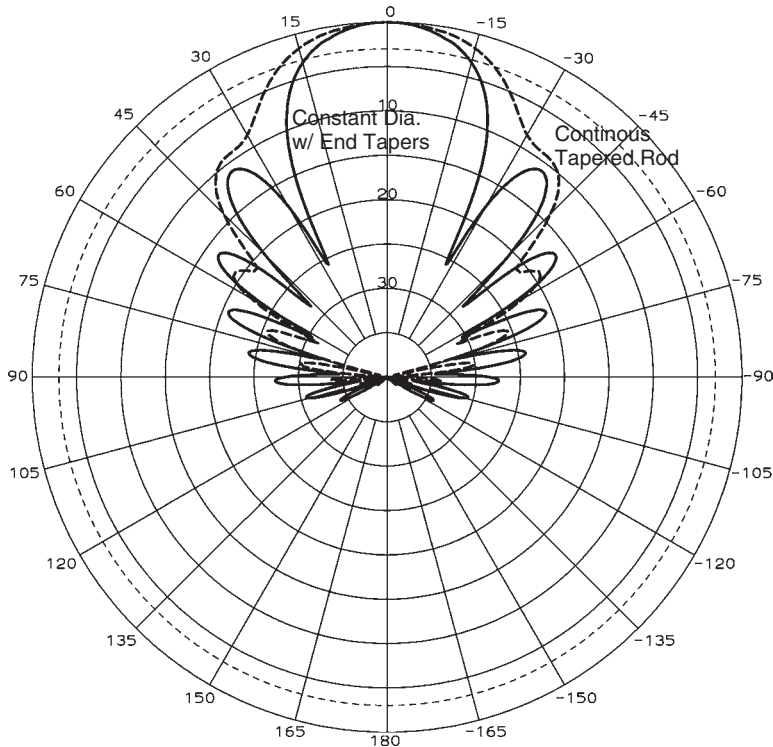


**FIGURE 10-16** Teflon rod antenna: constant diameter with short end tapers (solid line); continuous tapered rod (dashed line).

The filling factors are easily calculated:  $QF = 0.3138$  (Teflon) and  $QF = 0.2405$  (Delrin). When we use the filling factor, we calculate the losses: 0.074 dB (Teflon) and 0.29 dB (Delrin). The filling factor reduces the losses if the wave is traveling totally in the waveguide: 0.24 dB (Teflon) and 1.20 dB in Delrin. Because a large proportion of the power travels outside the rod, it is reasonable to use a lossy dielectric for the antenna.

Figure 10-16 shows the patterns of  $5\lambda$ -long Teflon rod antennas for two designs. The solid curve illustrates the pattern for an antenna with an initial taper  $0.4\lambda$  long between the  $0.822\lambda$  diameter and the constant  $0.516\lambda$  rod and a final taper  $0.15\lambda$  long to a  $0.42\lambda$  diameter. The dash curve is the pattern of an antenna with a continuous taper along the length from  $0.822\lambda$  to  $0.42\lambda$ . You can see that the first null fills in and the beamwidth increases. The Delrin rod design shows similar results. For short dielectric rod antennas we can use a continuous taper. The pattern for a design  $6\lambda$  long distorts completely with a continuous taper design.

## 10-6 HELICAL WIRE ANTENNA [13, Chap. 7]

We can excite a single wire wound in a helix to radiate an end-fire pattern on its axis for a circumference around one wavelength. The axial beam is circularly polarized in the same sense as the helix. In low-gain applications the antenna works over a 1.7 : 1

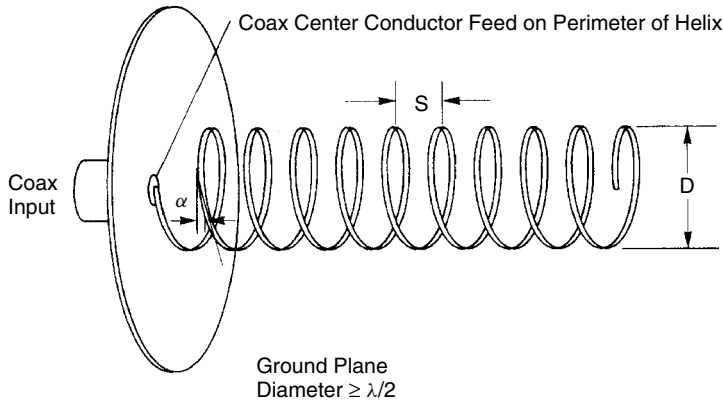


FIGURE 10-17 Axial mode helical wire antenna (RHC).

bandwidth that decreases as gain increases. We see this result from Figure 10-1 for any traveling-wave antenna. Figure 10-17 illustrates the parameters of a helical antenna. The helix has a pitch angle  $\alpha$  with spacing  $S$  on a diameter  $D$ . These parameters are interdependent.

$$\begin{aligned}
 C &= \pi D && \text{circumference} \\
 \tan \alpha &= \frac{S}{C} = \frac{S}{\pi D} \\
 L &= \sqrt{S^2 + C^2} = \frac{\pi D}{\cos \alpha} && \text{length of turn}
 \end{aligned} \tag{10-31}$$

### 10-6.1 Helical Modes

We arrive at an understanding of antenna operation by considering the modes of the helical transmission line. For diameters small in wavelengths, the wave travels along the wire at the free-space velocity in the  $T_0$  mode. This mode has equal phase points occurring on separate turns. Traveling-wave tube amplifiers use this mode to couple power from an electron beam. The helix slows the axial velocity of the wave by  $\sin \alpha$ .

The second mode,  $T_1$ , occurs when the circumference of the helix approaches one wavelength. The entire phase variation cycles on one turn. The velocity on the wire adjusts for the circumference in this mode. The adjustment gives a velocity whose axial component closely matches the Hansen and Woodyard criterion for increased end-fire directivity over a range of pitch angles.

The third helical transmission-line mode,  $T_2$ , has two cycles on each turn. The wave slows as compared with the  $T_1$  mode, but near a circumference of one wavelength, the  $T_1$  mode predominates. We express the general mode distribution by  $I_m e^{\pm jm\phi}$ , where  $m$  is an integer,  $\phi$  the polar angle of the developing helix, and the sign determines the polarization sense ( $-$  = right hand).

The  $T_1$  mode radiates its beam peak on the helix axis. The  $T_0$  mode radiates the normal mode, a dipole-shaped pattern, from a combination of small loops and short dipoles arrayed along the axis. It produces circular polarization over a narrow band of

frequencies. The  $T_2$  mode radiates a pattern with a shape like that of the traveling-wave current (Figure 10-5a) with a null on its axis.

### 10-6.2 Axial Mode

Antennas radiating from the  $T_1$  mode have good axial ratio, bandwidth, and the possibility of high gains over narrow bandwidths. Transitions such as the feed and helix end excite other helical transmission-line modes detected in their patterns, but proper construction reduces these anomalies. We analyze the pattern response from a linear array of single-turn helical antennas spaced at the pitch  $S$ . Each loop is a traveling-wave current element  $I_1 e^{\pm j\phi}$ , from  $I_m e^{\pm jm\phi}$ . We calculate the total pattern from pattern multiplication of the single-turn helical antenna and a uniform-amplitude linear array with the pattern

$$E_0 \frac{\sin(N\psi/2)}{N\psi/2} \quad (10-32)$$

where  $\psi = kS \cos \theta + \delta$ ,  $\delta$  is the phase shift between array elements, and  $N$  is the number of turns. The antenna currents satisfy the Hansen and Woodyard criterion in the range of circumferences  $0.78\lambda$  to  $1.33\lambda$ . We can excite the  $T_1$  mode over that entire band for short helices (lengths less than  $2\lambda$ ), but we can obtain it cleanly for only a limited bandwidth on long helices. The Hansen–Woodyard criterion determines the axial phase shift:  $-\delta = kS + (\pi/N)$ . Since the wave travels around the wire, we add  $2\pi$  to match the  $T_1$  mode. Along the wire we have

$$PkL = Pk\sqrt{C^2 + S^2} = kS + \frac{\pi}{N} + 2\pi \quad \text{or} \quad \frac{PL}{\lambda} = \frac{S}{\lambda} + 1 + \frac{1}{2N} \quad (10-33)$$

Given  $L = \pi D / \cos \alpha = C / \cos \alpha$ , we define  $C_\lambda = C/\lambda$  and substitute it into Eq. (10-33) to obtain the relative propagation constant along the wire a result verified by experiments:

$$\begin{aligned} \frac{PC_\lambda}{\cos \alpha} &= C_\lambda \tan \alpha + \frac{2N+1}{2N} \\ P &= \sin \alpha + \frac{[(2N+1)/2N] \cos \alpha}{C_\lambda} \end{aligned} \quad (10-34)$$

The pattern of a single turn determines polarization along the axis while the array determines the pattern shape. Figure 10-18 gives the pattern of a single turn of a helical antenna with the  $T_1$  traveling-wave current for a five-turn helix. We see a cross-polarization level on a boresight of less than 25 dB, but little front to back when we include both polarizations. The end-fire array forms the beam to produce the total pattern (Figure 10-19). The five-turn helical antenna has the same boresight polarization as the individual turn. The boresight axial ratio improves when we add turns by

$$\text{axial ratio} = \frac{2N+1}{2N} \quad (10-35)$$

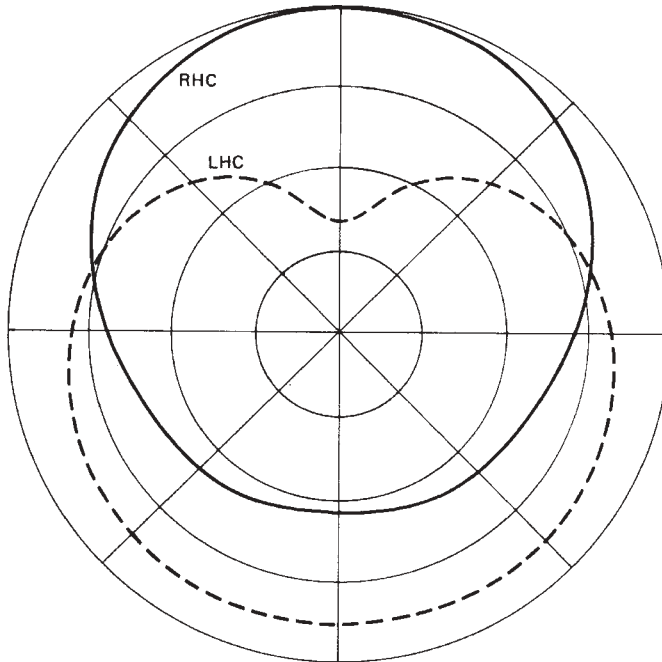


**FIGURE 10-18** Single turn of helical wire antenna with a circumference of  $0.9\lambda$  and  $\alpha = 13^\circ$ . The relative propagation constant  $P = 1.416$  on wire.

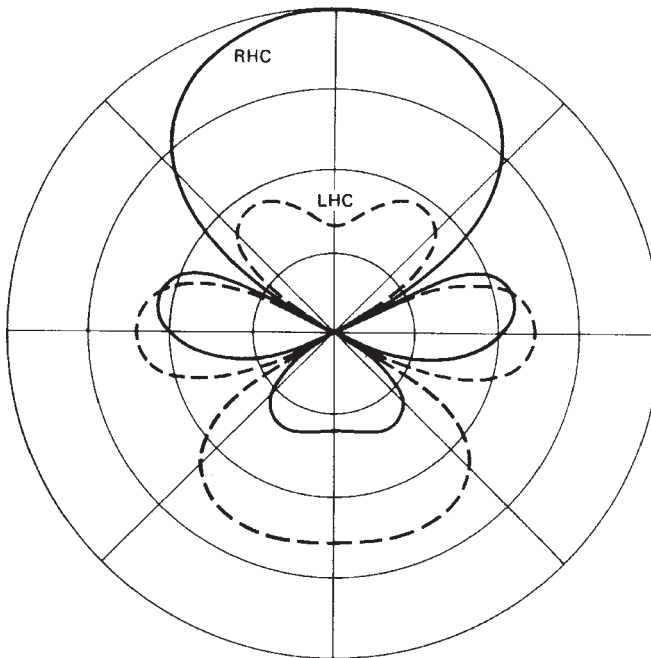


**FIGURE 10-19** Five-turn helical wire antenna with a circumference of  $0.9\lambda$  and  $\alpha = 13^\circ$ . The relative propagation constant  $P = 1.416$  on wire.



for current that follows the increased directivity criterion. The current wave rotates on the helix at nearly the radian frequency that approximately matches a circularly polarized wave. The helical antenna radiates the same sense of polarization as its screw sense. When looking into (from the beam peak) a helical antenna radiating RHC, the currents rotate counterclockwise.

The helical antenna operates best over the following limits:

$$\text{pitch angle: } 12^\circ \leq \alpha \leq 18^\circ \quad \text{circumference}/\lambda: 0.78 \leq C_\lambda \leq 1.33$$

Helical antennas can be built successfully outside the limits of  $\alpha$ . The diameter affects the possible directivity slightly, but we determine the directivity of the  $T_1$  mode mainly from the helix length. Figure 10-2 includes a plot of helix directivity. Exciting only the  $T_1$  mode becomes a problem as length increases because the feed region excites other helical transmission-line modes.

### 10-6.3 Feed of a Helical Antenna

We feed short helical antennas from a coax mounted on a ground plane that should be at least  $\lambda/2$  in diameter to achieve a good transition. The pattern does not depend on the ground plane to achieve good F/B because the five-turn helical antenna does not contain a ground plane. The antenna can be fed successfully from a coax twisted in a helix with the outer conductor tapered away in the manner of the split tapered coax balun (Section 5-15.9) until the center conductor alone feeds the helical antenna and a good F/B is achieved [30]. We place the coax feed on the edge of the helix and not on its axis, where an extra length transition must be made to the diameter. When the wire bends into the axis, it generates additional modes on the helix.

Kraus [13] gives an approximate formula for the helical antenna impedance:  $R = 141C_\lambda$ . The actual value varies about it. We reduce this impedance by soldering a flat strip on the wire from the feed of the helix [31]. The combination of the strip and the ground plane form a parallel-plate line that we space close together to form a tapered impedance transformer to produce a broadband low-impedance input. Empirical adjustments, by distorting the last half- to quarter-turn to taper wire spacing close to the ground plane, can also match the antenna to  $50 \Omega$  in a manner similar to the flat plate on the wire. We can design the transition by considering a flat sheet transmission line over a ground plane. The thickness of a dielectric sheet  $h$  and line width  $w$  necessary to match to the input impedance  $Z_0$  is given by [32, p. 234].

$$h = \frac{w}{(377/\sqrt{\epsilon_r}Z_0) - 2}$$

For narrowband applications we can use a gamma match feed (Section 5-13) to improve overall system performance. The long helical antenna is grounded and shunt fed. This prevents static charge buildup on the antenna and discharge through the receiver. The gamma match feed narrowbands the antenna and makes it act as a filter.

The feed configuration generates modes other than the  $T_1$  to satisfy the boundary conditions. Similarly, conditions on the end of the helical antenna also generate extra modes. Tapering the last two turns to a diameter 65% of the helix diameter reduces the mode generation from the end [33]. Tapering the diameter in the middle of the helix can also control the antenna's characteristics as we add degrees of freedom.

### 10-6.4 Long Helical Antenna

A long helical antenna can achieve the directivity predicted in Figure 10-2 over a limited bandwidth. The limited bandwidth comes not so much from the restrictions of Figure 10-1 (because the velocity on the helical transmission line adjusts to the length through coupling) as from the feed structure. Its structure generates extra modes whose radiation greatly reduces directivity. The normal flat ground-plane feed is limited to lengths of about  $2\lambda$ . Beyond that length the feed generates the  $T_0$  mode that radiates a broad pattern at  $\theta = 90^\circ$ .

A circular cup around the feed point (Figure 10-20) greatly reduces the excitation of unwanted modes. We determine the cup dimensions empirically. The dimensions given in Table 10-18 have been built or reported. In both cases the directivity fell by 0.2 dB from the curve for the Hansen and Woodyard criterion of Figure 10-2. The cup cannot fully eliminate the generation of extra modes on the helical antenna, since the pattern has dropped by about 0.5 dB from prediction because of the radiation of these extra modes. The 35-turn helical antenna has a 15% bandwidth, and the 50-turn helix has only a 10% bandwidth.

The helical transmission line fails to maintain the Hansen and Woodyard phase criterion over the total range of  $C_\lambda$  as the length increases. The lower values of  $C_\lambda$  retain this property, and the range of acceptable values shrinks as the number of turns increases. As the helix approaches infinite length, the range of acceptable  $C_\lambda$  values approaches 0.78 [35]. At 50 turns on a  $13^\circ$  pitch helical wire antenna, the proper phase velocity is maintained over the range  $0.78 \leq C_\lambda \leq 1.0$ .

Based on empirical data the peak gain can be expressed as an approximate formula in decibels [34]:

$$G_p = 8.3 \left( \frac{\pi D}{\lambda_p} \right)^{\sqrt{N+2}-1} \left( \frac{NS}{\lambda_p} \right)^{0.8} \left( \frac{\tan 12.5^\circ}{\tan \alpha} \right)^{\sqrt{N}/2}$$

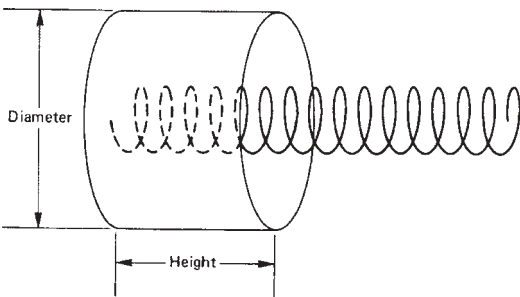


FIGURE 10-20 Cup feed for a long axial mode helical wire antenna.

TABLE 10-18 Cup Feed Dimensions for Long Helical Antennas

$N$	$\alpha$	$C$	$L$	Cup Diameter	Cup Height
35	$12.8^\circ$	$1.07\lambda$	$8.5\lambda$	$0.82\lambda$	$0.40\lambda$
50	$14^\circ$	$0.90\lambda$	$11.2\lambda$	$0.97\lambda$	$0.85\lambda$

Source: [34]

The peak gain occurs when  $\pi D/\lambda \sim 1.135$ . Given the ratio of gain to peak gain  $G/G_p$ , the frequency range ratio of high/low frequency is expressed as another empirical formula:

$$\frac{f_h}{f_l} = 1.07 \left( \frac{0.91}{G/G_p} \right)^{4/(3\sqrt{N})}$$

The beamwidth of a helical wire antenna has been expressed as an empirical formula [36]:

$$\text{HPBW} = \frac{K_B [2N/(N+5)]^{0.6}}{(\pi D/\lambda)^{\sqrt{N}/4} (NS/\lambda)^{0.7}} \left( \frac{\tan \alpha}{\tan 12.5^\circ} \right)^{\sqrt{N}/4}$$

Usual helixes have a constant  $K_B = 61.5^\circ$ , but helixes constructed on a dielectric rod require a different constant because the dielectric slows the wave on the helix.

### 10-6.5 Short Helical Antenna [37]

We can mount a short helical wire in a square cavity to make a conformal antenna. As shown in Figure 10-21, the helix has only two turns and the cavity depth is just sufficient for the helix height. The number of turns has minor effects on the pattern, determined primarily by the cavity width. Helixes with pitch angles from  $12$  to  $14^\circ$  give the best results when the cavity width is at least  $0.5\lambda$ . The pattern axial ratio improves for larger cavities, and the best results are obtained with an antenna on a flat ground plane. A cavity width of  $0.75\lambda$  gives good results, with its beamwidths ranging from  $45$  to  $60^\circ$ .

In the last quarter-turn we reduce the pitch angle to between  $2$  and  $6^\circ$  to form the tapered transformer to match the feed to  $50 \Omega$ . As with the longer helical antennas, we place the feed connection on the perimeter of the helix. Both the impedance match

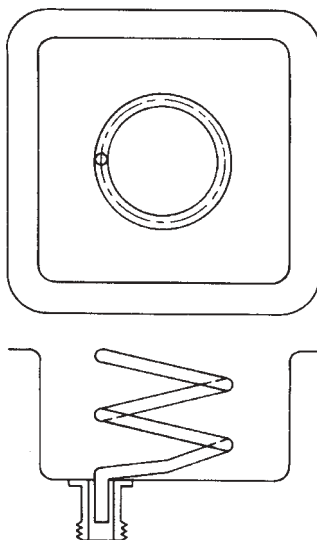


**FIGURE 10-21** Two-turn helical wire antenna in a cavity. [From [37], Fig. 1, © 1956 IRE (now IEEE).]

and pattern axial ratio improve compared with the central axis feed. The VSWR and pattern band extend from 0.9 to about 1.7 times the design frequency when the helix circumference is one wavelength. A two-turn helical antenna with a pitch angle of  $12^\circ$  has a cavity depth given by  $2\lambda \tan 12^\circ = 0.425\lambda$  for a one-wavelength helix circumference. This antenna is somewhat thicker than the antennas of Chapter 6, but the increased volume increases the bandwidth to nearly an octave.

## 10-7 SHORT BACKFIRE ANTENNA

A short backfire antenna consists of a round disk  $\approx 2\lambda$  diameter with a  $\lambda/4$  rim. A dipole (or crossed dipole) is mounted  $\lambda/4$  above the disk, and a second small disk  $\approx \lambda/2$  diameter is located  $\lambda/2$  above the lower disk [38]. The smaller disk acts as a semitransparent obstacle that reflects a portion of the radiation from the dipole. The large disk reflects the signal from the small disk and the ringing between the two increases the effective length of the antenna. This increases the gain to 12 to 14 dB. The general backfire consists of a slow-wave radiator pointed into a ground plane that causes ringing with the reflector element, for example, in a Yagi–Uda dipole antenna. Unfortunately, the short backfire has a bandwidth that ranges between 3 and 5%. Changing the large flat disk into a shallow cone and retaining the outer rim increases the bandwidth but reduces the gain a little [39]. Adding an extra director disk gives the extra parameter needed for impedance matching over a wider band.

Figure 10-22 shows side views of the normal and conical short backfire antennas. Often, the dipole is fed with a sleeve that attaches to a central tube used to support the director disk. We place the balun inside the tube and feed one or two dipoles. The sleeves cannot increase the bandwidth, but they raise the input resistance. Similar to a Yagi–Uda dipole antenna, the director and reflector disks lower the input

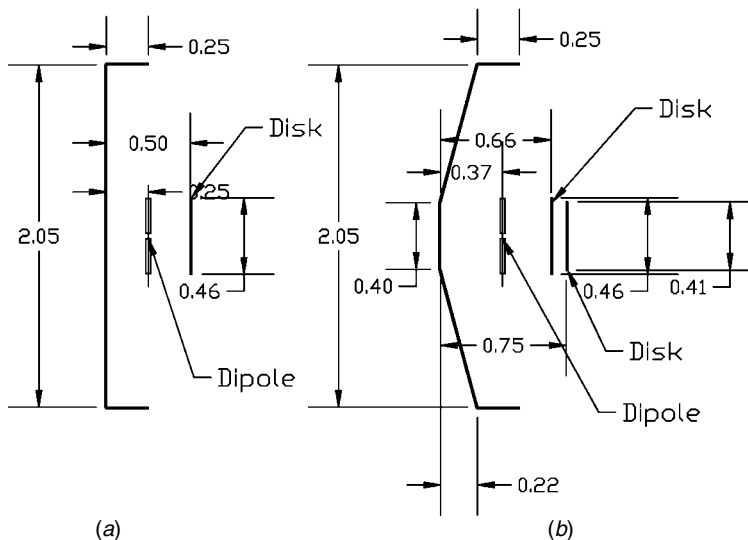


**FIGURE 10-22** Short backfire antenna with dimensions in  $\lambda$ : (a) original narrowband design; (b) conical wideband design.

impedance. The conical reflector increases the input resistance because the cone lowers the interaction between the two disks by reducing one reflection.

We could say that the conical back reflector approximates a parabola and explain its operation in that way, but the director disk is too small to produce an effective ground plane for the feed dipole. Figure 10-23 plots the pattern of the normal short backfire of Figure 10-22a when fed from a crossed dipole excited for RHC polarization in the direction of the director disk. The crossed dipole radiates LHC toward the  $2.05\lambda$ -diameter rimmed reflector that converts LHC to RHC upon reflection. Gain peaks at 14.2 dB, as shown, with a narrow beamwidth determined by the  $2.05\lambda$  diameter with an F/B ratio of 12 dB (LHC backlobe) and low sidelobes. The conical reflector ( $15^\circ$  cone, Figure 10-22b) pattern (Figure 10-24) has the same beamwidth as Figure 10-23, but has higher sidelobes and greater radiation in LHC polarization, which produced a pattern with 2 dB less directivity. Figure 10-25 plots the Smith chart of a conical short backfire, showing the dual resonance that produces a 1.6:1 VSWR bandwidth of 29%. For comparison a  $0.8\lambda$ -diameter disk was used as the feed dipole ground plane. Figure 10-26 gives the pattern of the comparison paraboloidal reflector with diameter  $2\lambda$  fed by a crossed dipole located over a  $0.8\lambda$ -diameter disk. We read Table 5-1 to determine a suitable reflector  $f/D$  (0.34) given the beamwidth and place the reflector focus at the phase center  $0.12\lambda$  above the ground plane. Gain drops to 10.8 dB because the feed and reflector combination radiates large spread-out sidelobes and significant cross-polarization, but its beamwidth matches that of short backfire antennas.

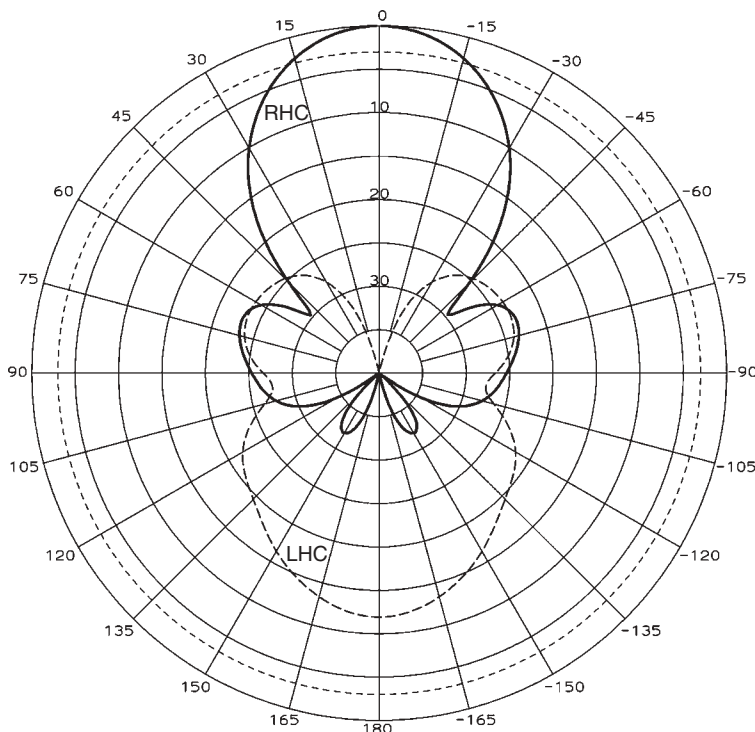


**FIGURE 10-23** Pattern of a short backfire antenna of Figure 10-22a with RHC crossed-dipole feed.

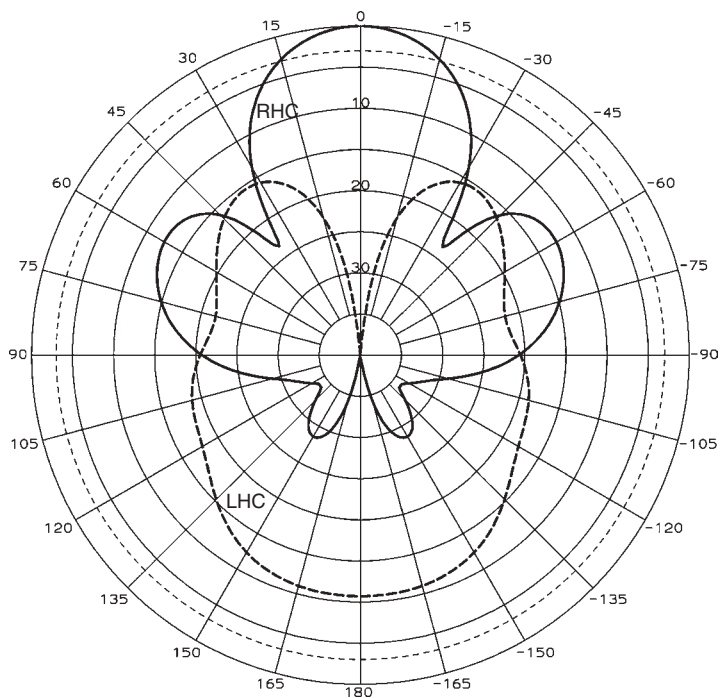


**FIGURE 10-24** Pattern of a conical short backfire antenna of Figure 10-22*b* with RHC crossed-dipole feed.

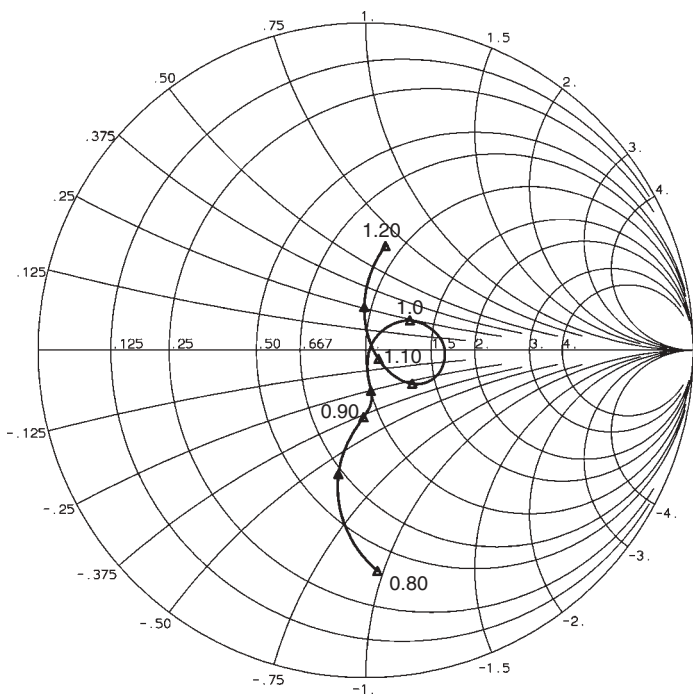


**FIGURE 10-25** Normalized impedance response of a conical short backfire antenna (Figure 10-22*b*).

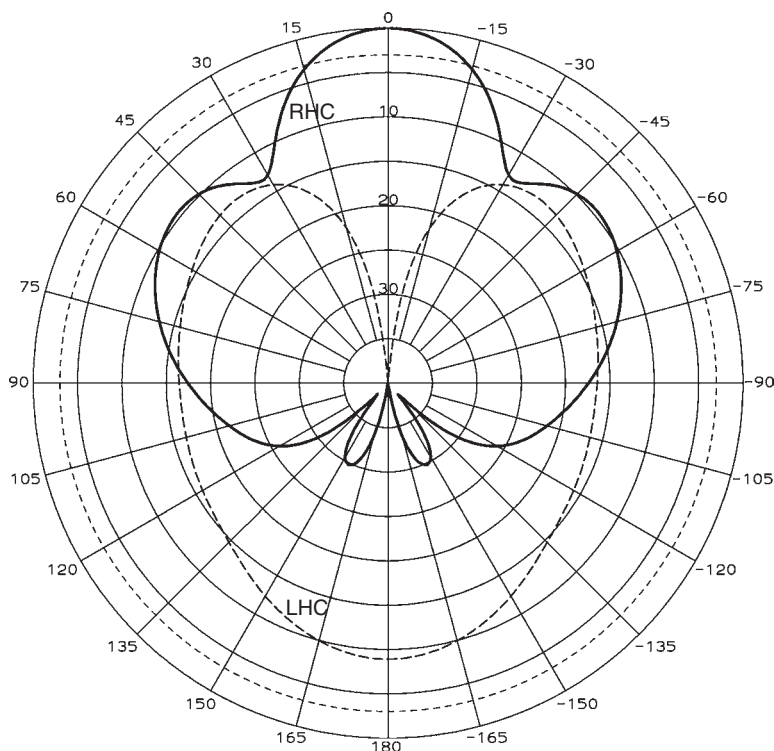


**FIGURE 10-26** Pattern of a  $2\lambda$ -diameter paraboloidal reflector  $f/D = 0.34$  with RHC crossed-dipole feed located over a  $0.8\lambda$ -diameter disk.

We cannot make significant changes to the pattern obtained from a short backfire antenna by varying its parameters. We increase gain by arraying these antennas, but we cannot scan the array because the narrow element beamwidth reduces gain rapidly with scan. Of course, the larger ground plane of the array reduces the backlobe, but in Figure 10-23 it only reduces gain by 0.28 dB. The simple construction is its advantage.

## 10-8 TAPERED SLOT ANTENNAS

A tapered slot antenna uses a flared slot line etched on a dielectric substrate to produce an end-fire pattern from a surface wave. A single element radiates this end-fire pattern over a wide bandwidth. When we combine a number of these elements in an array, their mutual coupling improves the impedance match when we space them closely. This unique property allows the construction of wide bandwidth arrays with both good impedance properties and the suppression of grating lobes.

Figure 10-27 illustrates four types of tapered slot antennas. The input at the bottom of the figure consists of either a coaxial-to-slotline transition or a fin-line in a waveguide that feeds into the slotline. In the slotline region the small gap binds the power to the transmission line, and as the transmission line slot widens, it radiates. Similar to the dielectric rod antenna, where we design the initial portion to have waves tightly bound to the rod, the slotline binds waves tightly to it. In the dielectric rod we

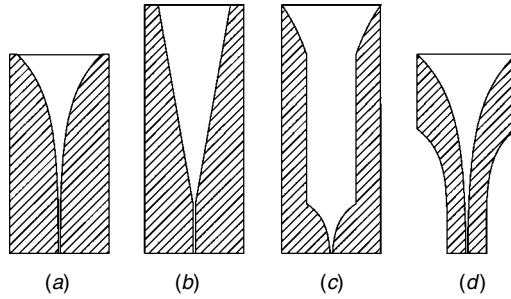


**FIGURE 10-27** Tapered slot antennas: (a) exponentially tapered slot antenna; (b) linear tapered slot antenna; (c) continuous-width slot antenna; (d) dual exponentially tapered slot antenna.

use a slow wave to attach the waves since values of  $P > 1$ , the relative propagation constant, cause a rapid attenuation of the fields for movement away from the surface. Instead of slowing the wave, we use the narrow gap of the slotline to bind the wave. Because the tapered slot is etched on a dielectric substrate, the wave is slowed on the slotline. Opening the slot increases radiation.

An exponentially tapered slot antenna (ETSA) [40], also called a *Vivaldi antenna*, radiates nearly equal  $E$ - and  $H$ -plane beamwidths that change only slightly as frequency increases. The input impedance match is good and the antenna radiates when the final width of the slot is  $\geq \lambda/2$ . At the lowest frequency the exponential taper is  $0.72\lambda$  long for an antenna etched on an alumina substrate. The antenna radiates a pattern with a  $180^\circ$   $H$ -plane beamwidth and a  $70^\circ$   $E$ -plane beamwidth for a  $\lambda/2$  aperture. For a  $\lambda$  aperture width it radiates  $E$ - and  $H$ -plane beamwidths of  $60^\circ$  and  $70^\circ$ . The two beamwidths are essentially the same for  $1.5\lambda$  and larger apertures:

Vivaldi antenna beamwidths, alumina substrate

Aperture ( $\lambda$ )	1.5	2	2.5	3	3.5	4	4.5	5	5.5	6
Beamwidths (deg)	50	42	38	33	31	30	30	30	32	35

The effective radiation region length combined with the substrate slowing determines the  $H$ -plane beamwidth of this slow-wave structure. Figure 10-2 shows that the antenna with an aperture of  $1.5\lambda$  and a length of  $2.2\lambda$  has its wave slowed by the dielectric to achieve a  $50^\circ$  beamwidth because without dielectric, slowing the beamwidth would be  $75^\circ$ . The flat and increasing beamwidth as frequency increases indicates that the radiation region shrinks. This means that the large slot widths radiate all the power in the wave before the end.

The antenna has high  $E$ -plane sidelobes on the order of  $-5$  dB. It appears that the antenna generates a surface wave in the dielectric because it has high cross-polarization that contains 20 to 30% of the radiated power, with its peak cross-polarization occurring in the diagonal plane. We can improve the cross-polarization by removing the dielectric in the slot region, but the beamwidth broadens because the dielectric no longer slows the wave. Even removing a portion, such as a rectangular notch, helps.

We excite this type of tapered slot antenna by using a microstrip-to-slotline transition. We etch a microstrip transmission line on the side opposite the slotted ground plane and run it across the slot. We can either connect the line to a via that runs to the other side of the slotted ground plane or connect it to a fan pattern that produces



a wide-bandwidth short circuit. The fan reduces fabrication cost because it is only an etched element. The open-circuited end of the slotline is terminated with a circular opening to produce a wide-bandwidth open circuit. Unfortunately, this connection generates a surface wave in the dielectric that radiates cross-polarization, due to the imbalance between the feed and the ground plane.

A linear tapered slot antenna (LTSA) radiates a higher gain pattern than that of an ETSA because it relies on length to narrow its beamwidth [41]. The opening angles of these antennas range from 5 to 12°. We use the development in Section 10-1 to determine the gain and beamwidth. The dielectric substrate slows the wave in the slot and increases gain. We calculate an effective dielectric thickness from the equation

$$\frac{t_{\text{eff}}}{\lambda} = (\sqrt{\epsilon_r} - 1) \frac{t}{\lambda}$$

The optimum values for  $t_{\text{eff}}/\lambda$  range between 0.005 and 0.03. Thinner substrates produce insufficient slowing, and thicker substrates produce too much slowing, which breaks up the main beam. Figure 10-28 plots the pattern of an LTSA with and without the dielectric in the tapered region. The pattern of the antenna containing the dielectric has broken up and has high sidelobes. Removing the dielectric increases the beamwidth while decreasing the sidelobes.

A continuous-width slot antenna (CWSA), is similar to a dielectric rod antenna. An initial short taper opens the slot to a uniform-width region where most of the radiation occurs. Sometimes the uniform region then opens to a wider region (Figure 10-27) that terminates the slotline. We design this antenna similar to a dielectric rod and determine its length by the desired gain. This antenna has the narrowest beamwidth and highest gain of the tapered slot antennas for a given length.

The final configuration in Figure 10-27 uses a dual exponential tapered slot (DETSA) to improve the impedance match. The bunny-ear version of this antenna achieves a 2:1 VSWR from 0.5 to 18 GHz [42]. This antenna uses a balanced slotline to reduce the cross-polarization. A balanced slotline has the same pattern etched on both sides of the substrate. The feed region consists of a stripline transition, which crosses both slots and is terminated in a centrally located fan to generate the short circuit. The balanced configuration prevents generation of a surface wave in the dielectric. The narrowed-width slotline ground plane improves the impedance match. Both the ground plane increases and the slot widens in the radiation region. The size and pattern of this antenna are similar to those of the Vivaldi, with a reduced mutual coupling because the substrate surface wave is eliminated.

Other feeding configurations of the tapered slot antenna include the antipodal Vivaldi antenna [43] and the balanced antipodal antenna [44]. These are not slot antennas but are similar in shape and performance to the Vivaldi antenna. The antipodal antenna places the two sides of the Vivaldi exponential taper on opposite sides of the substrate. We feed one side directly from the microstrip line and rapidly taper the ground plane symmetrically to form a twin plate line. To form the radiation portion, the twin plate line is spread into the dual exponentially radiator similar to a bunny-ear antenna. Unfortunately, the offset between the two sides causes significant cross-polarization, higher than that of the Vivaldi antenna, etched on a substrate. The advantage of the antenna is the easy transition from microstrip to radiator. By using a balanced antipodal design fed from a stripline, cross-polarization can be reduced while retaining the simple construction. This three-layer structure feeds one ear from the center conductor and

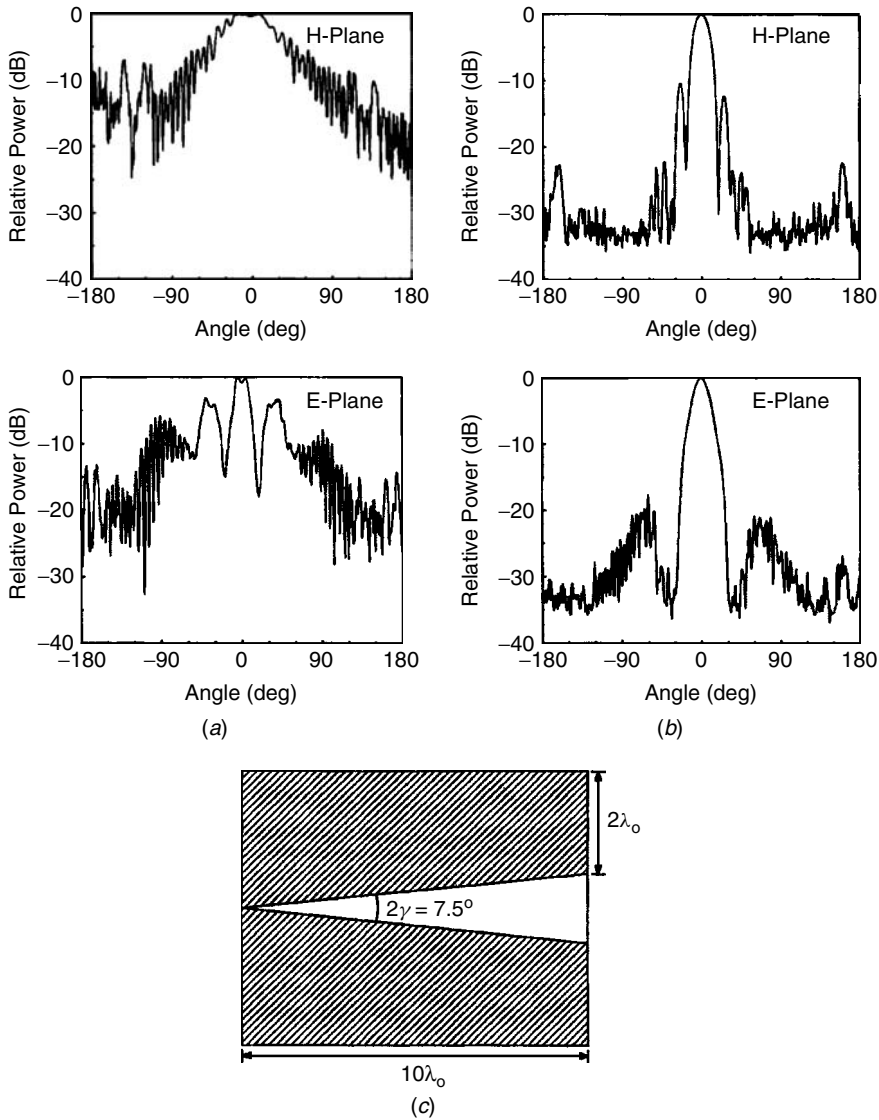


**FIGURE 10-28** LTSA patterns: (a) with  $\epsilon_r = 10$  substrate in slot; (b) without dielectric in slot; (c) outline of the antenna. (From [41], Fig. 5, © 1989 IEEE.)

balanced ears located on top of each other from the two ground planes. The design tapers the two ground planes until a balanced triplate line is formed before widening the center conductor and ground planes by using the dual exponential design. The balanced configuration reduces cross-polarization by 15 to 20 dB.

Tapered slot antennas have unique properties useful for wide bandwidth arrays. Although a single-element radiator requires the slot opening to be at least  $\lambda/2$ , in an array the mutual coupling allows this to be reduced to  $0.1\lambda$  [45]. The scan impedance produces a low-VSWR array measured to an array scan angle of  $50^\circ$  over a 5.9:1 bandwidth. Figure 10-29 shows an antenna built with tapered slot antennas in an egg

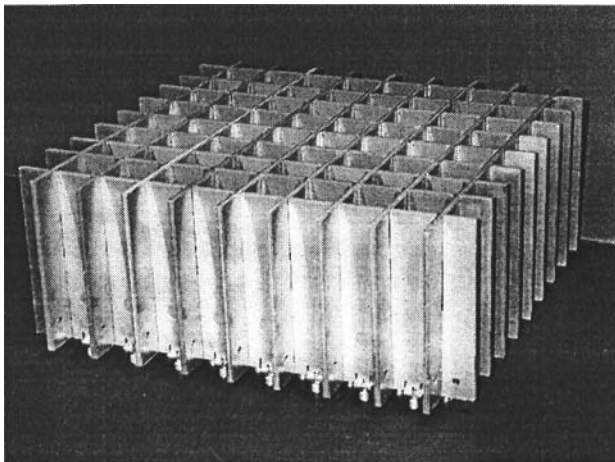


**FIGURE 10-29** Square array of 64 tapered slot antennas. (From [45], Fig. 1, © 2000 IEEE.)

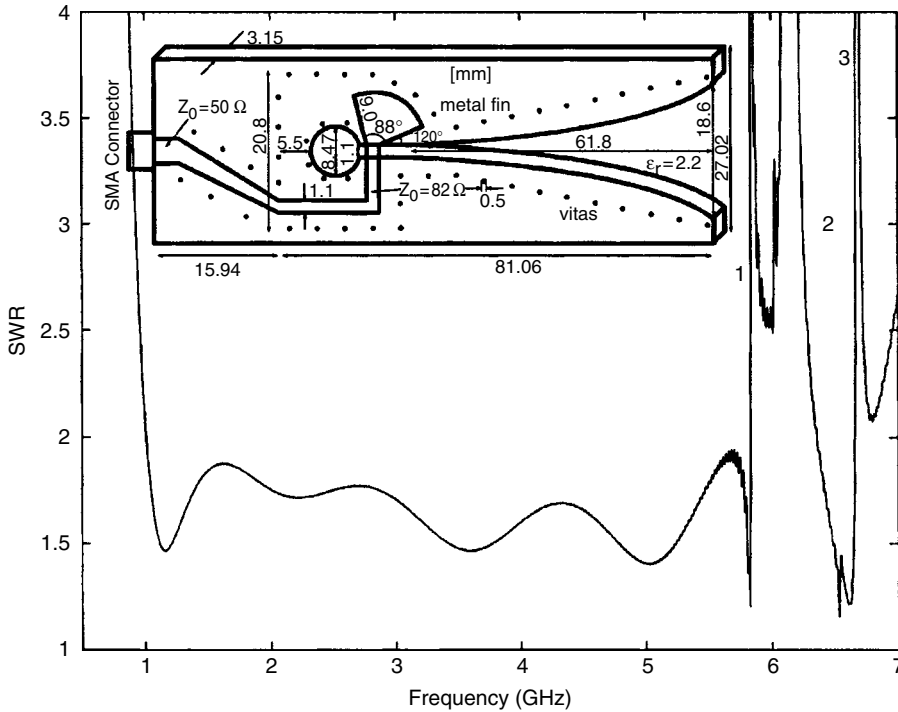
crate configuration to radiate dual linear polarization. To prevent grating lobes, the elements must be limited to a little larger than a  $\lambda/2$  separation at the highest operating frequency. Remember that the length of the antennas will not increase the element gain because it cannot exceed the effective area associated with each element. The length is to improve the impedance match and to increase the mutual coupling that allows the small slot widths.

Figure 10-30 illustrates construction of an ETSA element in the array. It uses a balanced slotline construction that has matching slots on both sides of the substrate. Halfway between the two sides a strip transmission line feeds the two slots when terminated by a fan that produces a short circuit. A circular open circuit etched in the two sides terminates the slotline. The stripline feeder contains a tapered transformer to transition between the  $50\text{-}\Omega$  input and the  $82\text{-}\Omega$  balanced slotline. The mutual coupling between the elements produces narrow-frequency bandwidth resonances in the array that can be suppressed by adding vias between the two sides of the balanced slotline along the edges and around the stripline feeder.

## 10-9 LEAKY WAVE STRUCTURES

A leaky wave structure allows for the separate specification of the amplitude distribution and beam direction. We position the beam direction by adjusting the relative propagation constant [Eq. (10-7)]. The surface-wave structure permits only small modifications of the amplitude distribution for the pattern scanned to end fire. The uniform distribution on an axisymmetrical leaky wave structure has a directivity of  $2L/\lambda$  independent of scan angle until the pattern approaches end fire. Near end fire the cone beamwidths join to produce higher directivities. Figure 10-1 shows the modification of directivity as these join ( $P \rightarrow 1$ ). The directivity is nearly constant below  $P = 0.9$  for lengths  $8\lambda$  and  $10\lambda$ .

Tapered amplitude distributions reduce directivity by the amplitude taper efficiency [Eq. (4-6)]. The relative propagation constant along the structure determines the beam



made into a leaky wave antenna by openings that cut the wall currents. For example, a slot in the center of the broadwall of a rectangular waveguide does not radiate because it cuts no net current. If we vary the distance of a continuous slot from the centerline, we can control the leakage rate. We form other leaky wave antennas by cutting closely spaced holes or slots. We analyze these discrete radiators as continuous structures whose radiation rate is controlled by the size of the holes or the placement of the slots.

## REFERENCES

1. W. W. Hansen and J. R. Woodyard, A new principle in antenna design, *Proceedings of IRE*, vol. 26, no. 3, March 1938, pp. 333–345.
2. C. H. Walters, *Traveling Wave Antennas*, Dover, New York, 1970.
3. H. W. Ehrenspeck and H. Poehler, A new method for obtaining maximum gain from Yagi antennas, *IRE Transactions on Antennas and Propagation*, vol. AP-7, no. 4, October 1959, p. 379.
4. F. J. Zucker, Chapter 16 in H. Jasik, ed., *Antenna Engineering Handbook*, McGraw-Hill, New York, 1961.
5. R. F. Harrington, *Time-Harmonic Electromagnetic Fields*, McGraw-Hill, New York, 1961.
6. H. H. Beverage, C. W. Rice, and E. W. Kellogg, The wave antenna: a new type of highly directive antenna, *AIEE Transactions*, vol. 42, 1923, p. 215.
7. K. Lizuka, The traveling-wave V-antenna and related antennas, *IEEE Transactions on Antennas and Propagation*, vol. AP-15, no. 2, March 1967, pp. 236–243.
8. G. A. Thiele and E. P. Ekelman, Design formulas for vee dipoles, *IEEE Transactions on Antennas and Propagation*, vol. AP-28, no. 4, July 1980, pp. 588–590.
9. A. E. Harper, *Rhombic Antenna Design*, Van Nostrand, New York, 1941.
10. H. Yagi, Beam transmission of ultra short waves, *Proceedings of IRE*, vol. 26, June 1928, pp. 715–741.
11. R. J. Mailloux, Antenna and wave theories of infinite Yagi–Uda arrays, *IEEE Transactions on Antennas and Propagation*, vol. AP-13, no. 4, July 1965, pp. 499–506.
12. P. S. Carter, Circuit relations in radiating systems and applications to antenna problems, *Proceedings of IRE*, vol. 20, 1932, p. 1004.
13. J. D. Kraus, *Antennas*, McGraw-Hill, New York, 1950.
14. R. C. Hansen, ed., *Microwave Scanning Antennas*, Vol. II, Academic Press, New York, 1966.
15. H. E. King, Mutual impedance of unequal length antennas in echelon, *IRE Transactions on Antennas and Propagation*, vol. AP-5, July 1957, pp. 306–313.
16. J. H. Richmond, Coupled linear antennas with skew orientation, *IEEE Transactions on Antennas and Propagation*, vol. AP-18, no. 5, September 1970, pp. 694–696.
17. C. A. Thiele, Analysis of Yagi–Uda type antennas, *IEEE Transactions on Antennas and Propagation*, vol. AP-17, no. 1, January 1969, pp. 24–31.
18. D. K. Cheng and C. A. Chen, Optimum element spacings for Yagi–Uda arrays, *IEEE Transactions on Antennas and Propagation*, vol. AP-21, no. 5, September 1973, pp. 615–623.
19. C. A. Chen and D. K. Cheng, Optimum element lengths for Yagi–Uda arrays, *IEEE Transactions on Antennas and Propagation*, vol. AP-23, no. 1, January 1975, pp. 8–15.
20. D. Kajfez, Nonlinear optimization extends the bandwidth of Yagi antenna, *IEEE Transactions on Antennas and Propagation*, vol. AP-23, no. 2, March 1975, pp. 287–289.
21. P. P. Vezibicke, Yagi antenna design, *NBS Technical Note 688*, U.S. Department of Commerce/National Bureau of Standards, December 1976.

22. W. K. Kahn, Double ended backward-wave Yagi hybrid antenna, *IEEE Transactions on Antennas and Propagation*, vol. AP-29, no. 3, May 1981, pp. 530–532.
23. J. E. Lindsay, A parasitic endfire array of circular loop elements, *IEEE Transactions on Antennas and Propagation*, vol. AP-15, no. 5, September 1967, pp. 697–698.
24. L. C. Shen and G. W. Raffoul, Optimum design of Yagi array of loops, *IEEE Transactions on Antennas and Propagation*, vol. AP-22, no. 6, November 1974, pp. 829–831.
25. A. Shoamanesh and L. Shafai, Design data for coaxial Yagi array of circular loops, *IEEE Transactions on Antennas and Propagation*, vol. AP-27, no. 5, September 1979, pp. 711–713.
26. S. A. Brunstein and R. F. Thomas, Characteristics of a cigar antenna, *JPL Quarterly Technical Review*, vol. 1, no. 2, July 1971, pp. 87–95.
27. J. L. Wong and H. E. King, A wide-band low-sidelobe Disc-o-Cone antenna, *IEEE Transactions on Antennas and Propagation*, vol. AP-31, no. 1, January 1983, pp. 183, 184–.
28. V. C. Smits, Rear gain control of a dielectric rod antenna, *Microwave Journal*, vol. 11, no. 12, December 1968, pp. 65–67.
29. S. Kobayashi, R. Mittra, and R. Lampe, Dielectric tapered rod antennas for millimeter applications, *IEEE Transactions on Antennas and Propagation*, vol. AP-30, no. 1, January 1982, pp. 54–58.
30. B. A. Munk and L. Peters, A helical launcher for the helical antenna, *IEEE Transactions on Antennas and Propagation*, vol. AP-16, no. 3, May 1968, pp. 362–363.
31. J. D. Kraus, A 50-ohm input impedance for helical beam antennas, *IEEE Transactions on Antennas and Propagation*, vol. AP-25, no. 6, November 1977, p. 913.
32. J. D. Kraus and R. J. Marhefka, *Antennas for All Applications*, 3rd ed., McGraw-Hill, New York, 2003.
33. J. L. Wong and H. E. King, Broadband quasi-taper helical antennas, *IEEE Transactions on Antennas and Propagation*, vol. AP-27, no. 1, January 1979, pp. 72–78.
34. H. E. King and J. L. Wong, Characteristics of 1 to 8 wavelength uniform helical antennas, *IEEE Transactions on Antennas and Propagation*, vol. AP-28, no. 3, March 1980, pp. 291–296.
35. T. S. M. Maclean and R. G. Kouyoumjian, The bandwidth of helical antennas, *IRE Transactions on Antennas and Propagation, Symposium Supplement*, vol. AP-7, December 1959, pp. S379–S386.
36. J. L. Wong and H. E. King, Empirical helical antenna design, *Digest of the International Symposium on Antennas and Propagation*, 1982, pp. 366–369.
37. A. Bystrom and D. G. Berntsen, An experimental investigation of cavity-mounted helical antennas, *IRE Transactions on Antennas and Propagation*, vol. AP-4, no. 1, January 1956, pp. 53–58.
38. H. W. Ehrenspeck, The short backfire antenna, *Proceedings of IEEE*, vol. 53, no. 4, August 1965, pp. 1138–1140.
39. S. Ohmori et al., An improvement in electrical characteristics of a short backfire antenna, *IEEE Transactions on Antennas and Propagation*, vol. AP-31, no. 4, July 1983, pp. 644–646.
40. P. J. Gibson, The Vivaldi aerial, *Proceedings of the 9th European Microwave Conference*, Brighton, East Sussex, England, 1979, pp. 101–105.
41. K. S. Yngvesson et al., The tapered slot antenna: a new integrated element for millimeter-wave applications, *IEEE Transactions on Microwave Theory and Techniques*, vol. 37, no. 2, February 1989, pp. 365–374.
42. J. J. Lee and S. Livingston, Wide band bunny-ear radiating element, *IEEE AP-S Symposium*, 1993, pp. 1604–1607.

- 43. E. Gazit, Improved design of the Vivaldi antenna, *IEE Proceedings*, vol. 135, pt. H, no. 2, April 1988, pp. 89–92.
- 44. J. D. S. Langley, P. S. Hall, and P. Newham, Novel ultrawide-bandwidth Vivaldi antenna with low cross polarization, *Electronics Letters*, vol. 29, no. 23, November 11, 1993, pp. 2004–2005.
- 45. H. Holter, T. -H. Chio, and D. H. Schaubert, Experimental results of 144-element dual-polarized endfire tapered-slot phased arrays, *IEEE Transactions on Antennas and Propagation*, vol. 48, no. 11, November 2000, pp. 1707–1718.